

Chapter 3

BUOYS

In case of buoy measurements, the wave directional spectrum is determined from the simultaneous time series measurements of wave elevation (obtained by double integration of the vertical acceleration, i.e., the heave signal), slopes of the wave surface in two mutually perpendicular directions (measured with inclinometers), and the compass orientation of the buoy. Such buoys are known as slope following buoys and were first used by Longuet-Higgins et al. [1963]. Buoys that measure the orbital velocity in two mutually perpendicular directions instead of the slope, known as orbital following buoys, are described by Middleton and LeBlanc [1982] and marketed by ENDECO.

The advantage of buoys over arrays is that buoys can be deployed both in deep water as well as shallow water. Also buoys can be very easily deployed, while a lot of logistic support, including diving and precise location of gauges, is required for installing and maintaining arrays.

3.1 FREQUENCY DOMAIN FILTER METHOD FOR DETERMINING WAVE DIRECTION FROM AN ORBITAL FOLLOWING BUOY

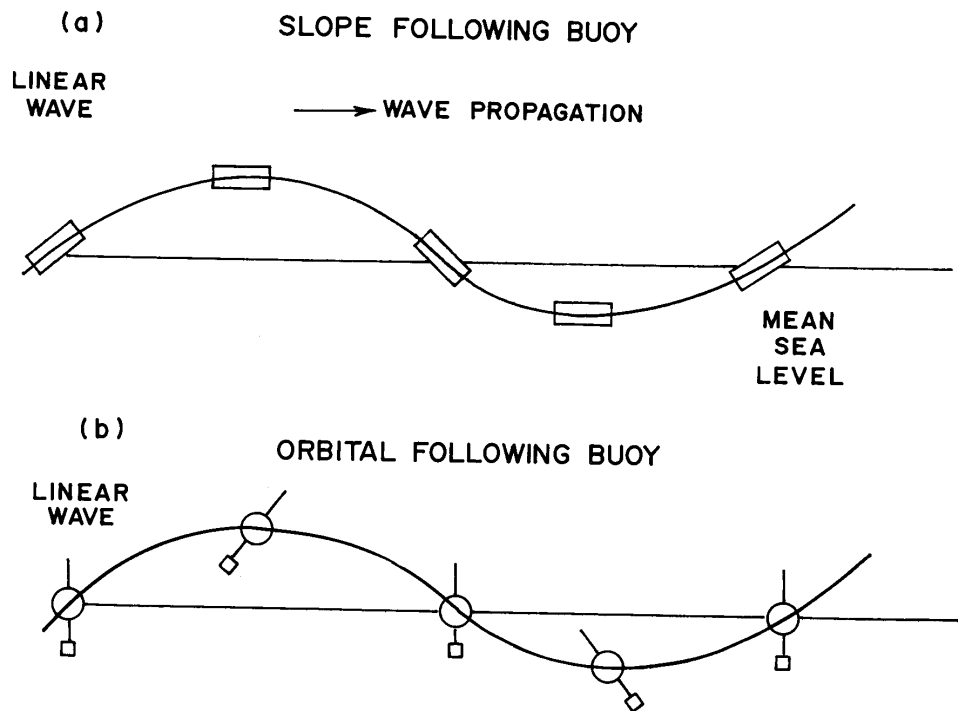
Software has been developed in FORTRAN language using a personal computer for the determination of wave direction from time series measurements of heave, pitch and roll of an orbital following buoy. The method of digital band pass filtering described by Edward C. Brainard II of Endeco Inc. USA was used. A derivation of the basic formula used is presented. The software developed by us, viz. BUOY-D-P.FOR, and the software provided by ENDECO, viz. 1156DBP.EXE, were both run for observed as well as computed simulated data. This is a preliminary report on program development. In the case of observed data, wave directions obtained with BUOY-D-P agreed within $\pm 5^\circ$ with the single available visual estimate of swell direction and within $\pm 5^\circ$ with directions obtained with 1156DBP. In the case of computer simulated data, BUOY-D-P was

able to recover wave directions accurately for both mono-chromatic and multi-chromatic wave trains. 1156DBP was equally successful, except that if the simulated wave direction was θ , the computed direction was found to be $\pi + \theta$. This offset has been explained.

3.1.1 Introduction

For the determination of wave direction, two types of wave following buoys are used, viz. slope following buoys and orbital following buoys. In the case of a slope following buoy, the tilt of the buoy in the direction of the wave follows a simple harmonic motion having the frequency of the wave and is 90° out of phase with the wave motion (also with heave of the buoy) (Figure 3.1a). Maximum tilt (positive and negative) is experienced on the slope of the wave at mean sea level. The buoy is level as the wave crest and trough. A slope following buoy has an inherent defect owing to its flat bottom “discus” shaped design. It is liable to capsize unless its diameter is larger (above 12 m). This type of buoy is also liable to give erroneous wave directions in the presence of breaking waves.

Figure 3.1 Slope and orbital following buoy motions



In the case of orbital following buoy, its tilt in the direction of the wave again follows a simple

harmonic motion having the frequency of the wave but is in phase with the wave motion (also with heave of the buoy), (Figure 3.1b). Maximum tilt (positive and negative) of the buoy occurs on the crest and trough of the wave. The buoy is level on the slope of the wave at mean sea level. This type of buoy is spherical in design, has a deeply suspended and rigidly attached ballast, behaves like an “inverted pendulum”, is inherently stable and cannot capsize. Also, breaking waves cannot introduce errors in the computation of wave direction.

Slope following buoys detect the vertical acceleration and the wave slope in the north-south and east-west directions. Tilt following buoys detect the vertical acceleration and the tilt of the buoy in the north-south and east-west direction. In both types of buoys, therefore, three independent measurements are made.

Slope following buoys came into existence first, and orbital following buoys came much later. The first slope following buoy was that of Longuet-Higgins et al. [1963] while perhaps the first orbital following buoy was that of Middleton et al. [1978]. The methodology created for the determination of the directional spectrum from the motions of a slope following buoy is being applied for orbital following buoys with slight modifications.

3.1.2 Methodology

Consider a one-dimensional mono-chromatic wave

$$h(t) = (H/2) \cos(\kappa x - \sigma t) \quad (3.1)$$

where h is the wave elevation with respect to time; H , the wave height; $\kappa (= 2\pi/L)$, the wave number; L , the wave length; $\sigma (= 2\pi/T)$, the angular frequency; and T , the wave period.

Let $z = 0$ be the mean water line, the z -axis reckoned positive upwards, and d be the mean water depth. Then the horizontal component of orbital velocity, u , and the vertical component of fluid acceleration, a_z due to the wave motion are given by:

$$u = \frac{\pi H}{T} \frac{\cosh[\kappa(z+d)]}{\sinh(\kappa d)} \cos(\kappa x - \sigma t) \quad (3.2)$$

$$a_z = -\frac{g\pi H}{L} \frac{\sinh[\kappa(z+d)]}{\cosh(\kappa d)} \cos(\kappa x - \sigma t) \quad (3.3)$$

Ideally, an orbital following buoy simultaneously performs two motions heave and tilt. Due to flotation, the buoy faithfully heaves up and down with the wave, i.e. it acts as a wave rider. And due to the horizontal component of orbital velocity, the buoy tilts positively and negatively in the direction of the wave, the tilt being proportional to the horizontal component of the orbital

velocity, u . The tilt of the buoy is in phase with the wave elevation because of the presence of $+\cos(kx - \sigma t)$ in (3.1) and (3.2).

As far as the tilt motion is concerned, the buoy acts as an inverted pendulum. This is achieved in practice by rigidly attaching to the buoy a deeply suspended ballast. The ballast acts as the fulcrum of the inverted pendulum, while the spherical buoy acts as the bob of the pendulum.

Due to the similarity between (3.1) and (3.3), the wave elevation is reckoned from the vertical acceleration of the buoy measured with an accelerometer. To determine the wave direction, besides the wave elevation, it is necessary to know the tilts of the buoy in the north-south and east-west directions. Two inclinometers measure the tilt in two mutually perpendicular directions with respect to the lubber's line on the buoy. These tilts, known as pitch and roll, are then converted into north-south and east-west tilts with the help of a two-axis flux gate compass. In the ENDECO system, the accelerometer, the two inclinometers and the two-axis flux gate compass are housed in the ballast of the buoy, while the electronics and the battery power supply are located in the spherical buoy.

We shall now present a derivation of the formula for the determination of wave direction from time series measurements of wave elevation (heave), north-south tilt and east-west tilt of the buoy for a mono-chromatic wave. It is assumed that:

a) Let θ be the wave direction. The wave direction is the direction from which the wave front comes, and is reckoned clockwise positive with respect to the north axis.

b) Let $h(t) = H \cos(\frac{2\pi t}{T} + \delta)$

where h is the wave elevation as a function of time t ; H , the amplitude of the wave; T , the period of the wave; and δ , the initial phase of the wave. Then the tilt of the buoy in the direction of wave is given by

$$\phi(t) = \frac{cH}{T} \cos(\frac{2\pi t}{T} + \delta)$$

where c is a constant. A positive tilt indicates that the buoy is tilted towards the direction in which the wave front is going, while a negative tilt indicates that the buoy is tilted towards the direction from which the wave front is coming.

Case (i) [$\phi(t) < 0$]: In Figure 3.2, θ is the wave direction; ϕ , the tilt of the buoy, and $P(x,y,z)$ is a point on the axis of the buoy. X-axis is along east, Y-axis along north and Z-axis vertically upwards. O is the lower extremity of the buoy; it is the point about which the buoy is tilting, i.e., the fulcrum. Note that since $\phi < 0$, the buoy is tilted towards the direction from which the wave front is coming. Then the north-south tilt, η , and the east-west tilt, ϵ , of the buoy are given by:

$$(N - S) : \tan \eta = \frac{r \sin |\phi| \cos \theta}{r \cos |\phi|} = \frac{y}{z}$$

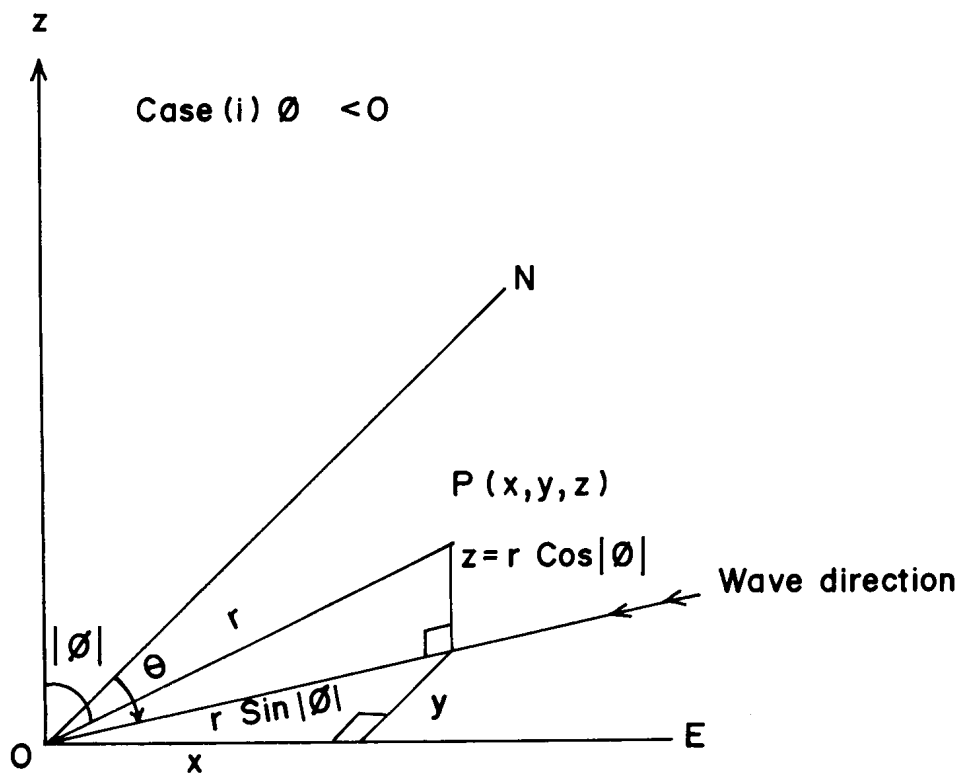
$$(E - W) : \tan \epsilon = \frac{r \sin |\phi| \sin \theta}{r \cos |\phi|} = \frac{x}{z}$$

And from the above two equations,

$$\theta = \arctan\left[\frac{\tan \epsilon}{\tan \eta}\right] \tag{3.4}$$

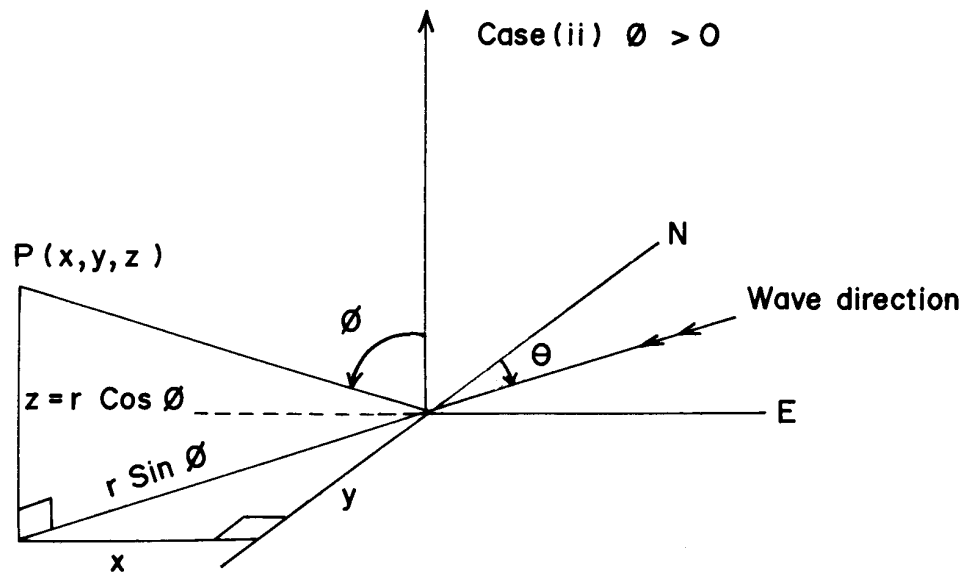
By taking into consideration the signs of the numerator and denominator, θ is uniquely determined in the range $(0, 2\pi)$. In FORTRAN programming language, this is conveniently achieved by invoking the double argument function ATAN2 (Y,X).

Figure 3.2 Buoy tilts for wave troughs



Case (ii) [$\phi(t) > 0$]: This case is treated in Figure 3.3. Note that since $\phi > 0$, the buoy is tilted towards the direction in which the wave front is going. In this case, the north-south tilt, η , and the east-west tilt, ϵ , are given by

Figure 3.3 Buoy tilts for wave crests



$$(N - S) : \tan \eta = \frac{r \sin \phi \cos(\theta + \pi)}{r \cos(\phi)} = \frac{y}{z}$$

$$(E - W) : \tan \epsilon = \frac{r \sin \phi \sin(\theta + \pi)}{r \cos(\phi)} = \frac{x}{z}$$

And from the above two equations,

$$\theta = \arctan\left[\frac{-\tan \epsilon}{-\tan \eta}\right] \quad (3.5)$$

By taking into consideration the signs of the numerator and denominator, θ is determined correctly and uniquely in the range $(0, 2\pi)$. It may be noted that since θ is determined in the range $(0, 2\pi)$ and not $(-\pi/2, \pi/2)$, (3.4) and (3.5), though similar, are two quite distinct formulae. It is also to be noted that (3.5), which is valid for all $\phi > 0$, is particularly valid for wave crests.

Brainard [????] has given the following formula for wave crests:

$$\theta = \arctan(\epsilon/\eta)$$

It may be noted that the above formula is an approximation of (3.5) that holds true for small values of η and ϵ , which generally is the case in practice. As we shall see later, the absence of the negative sign in the numerator and denominator is due to Brainard taking an inverted heave series as input for his computer program.

(3.4) and (3.5), are valid for monochromatic waves. The method of digital band-pass filtering assumes that these equations will be valid for high resolution spectral bands. Essentially, the method applies a band-pass filter to the heave, north-south tilt and east-west tilt series and uses (3.5) at each wave crest of the filtered series to determine the mean wave direction in the band.

Our software, viz. BUOY-D-P.FOR, runs in the manner indicated below: First, steps (1)-(3) are carried out. Then for each frequency band, steps (4)-(10) are performed. this is the main phase of the computations, as the mean wave direction and standard deviation of direction for each band are computed here. Lastly, in steps (11)-(13), the mean energy in each frequency band is computed and the essential results of the processing are printed.

- 1) Read heave, north-south tilt, and east-west tilt series, h,n,e respectively.
- 2) Perform FFT of h,n,e to obtain the Fourier transforms H,N,E respectively.
- 3) Save H,N,E in binary scratch files. Binary files are used for fast access.
- 4) *Read H,N,E.

- 5) *Band pass H,N,E, i.e. set the Fourier components outside the band to zero.
- 6) *Perform inverse FFT of H,N,E to obtain h,n,e.
- 7) *Determine the location of wave crests of h.
- 8) *Determine values of n and e corresponding to the wave crests.
- 9) *Determine the wave direction at each crest using (3.5).
- 10) *Determine the mean direction and standard deviation for the frequency band.
- 11) Use Blackman window on the original heave series.
- 12) Perform FFT of heave series.
- 13) Find mean energy in each band and scale the mean energy by a factor of 1/0.303 to compensate for loss of energy due to windowing.

3.1.3 Results and discussion

Our software, viz. BUOY-D-P.FOR, and the software provided by ENDECO, viz. 1156DBP.EXE, were both run for observed as well as computer simulated data. The observed data came from an ENDECO type 1156 directional wave-track buoy system deployed for eight days off Candolim, Goa (lat. 15° 30'N; long. 73° 44'E) in a mean water depth of 14 m. Low wave conditions prevailed during the entire period. The significant wave height was in the range 0.53-0.96 m and the zero crossing period was in the range 4.36-5.99 sec. There were two main spectral peaks, one generally around 11.11 sec and the other around 5.56 sec, the latter peak being the more dominant nearly all the time.

In Figure 3.4 are presented the mean directions at the peak frequency for two series of observed data: (i) 3 hourly records for one day from 1500 hrs on 5 March 1992, and (ii) 24 hourly records for 8 days from 12 hours on the same day. The figure shows that both the software show the same trends. The software 1156DBP shows more stable and perhaps more realistic wave directions. Directions computed by BUOY-D-P are within $\pm 50^\circ$ from those computed by 1156DBP.

At 1100 hrs on 10 March 1992, the swell direction was roughly estimated at 300° by visual observation. The results from two software for the record at 1200 hrs on the same day are presented in Table 3.1. It is seen that at the peak frequency (0.19 Hz), BUOY-D-P shows a mean wave direction of 325°, while 1156DBP shows the direction to be 302°. Both computed directions are close to the visual estimate. The data in Table 3.1 also show that the mean direction is more or less the same for all frequency bands in the case of BUOY-D-P. In the case of 1156DBP, wave directions show more scatter, specially at the low frequency end of the spectrum. This feature was noticed for all other records also.

The results obtained with the two software in the case of computer simulated data are discussed below. The characteristics of one record of simulated data are discussed below. The characteristics

Figure 3.4 Mean wave direction at peak frequency for (a) 3 hourly records, and (b) 24 hourly records

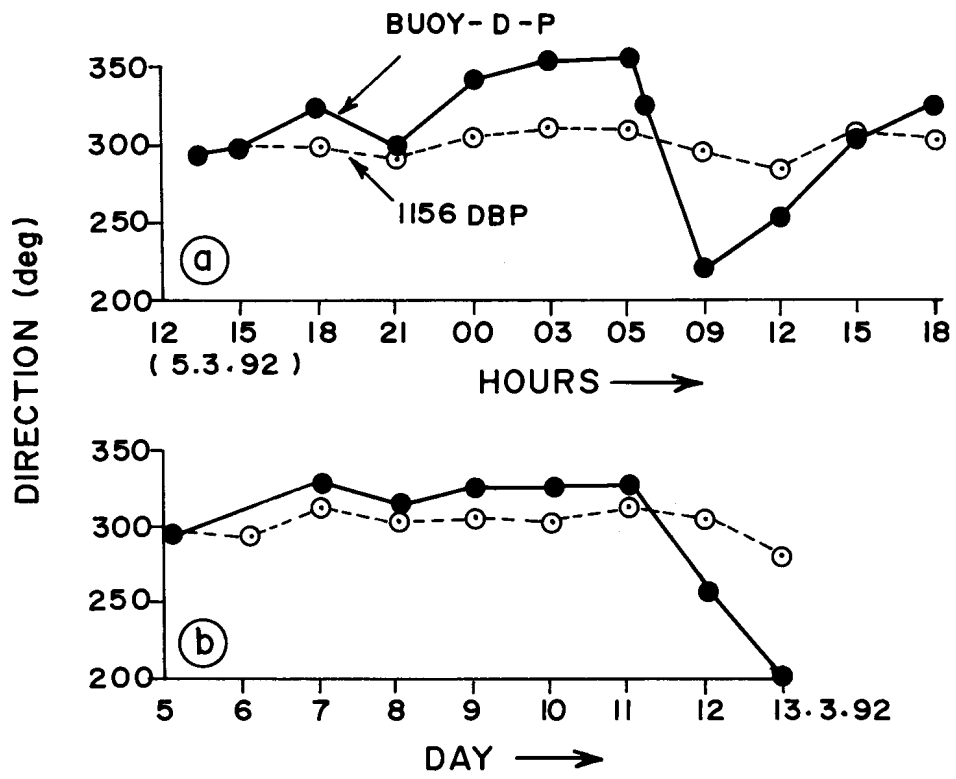


Table 3.1 Analysis of observed wave data using ENDECO wave directional orbital following buoy. Observation date, 10 March 1992; No. of points, 2048; sampling interval, 0.5 sec

Band No.	Centre Frequency (Hz)	Centre Period (sec)	Software BUOY-D-P			Software 1156DBP		
			Energy (m^2/Hz)	Dir (deg)	Std Dev (deg)	Energy (m^2/Hz)	Dir (deg)	Std Dev (deg)
1	0.03	33.33	0.06	325	003	0.10	350	012
2	0.04	25.00	0.08	321	002	0.11	001	008
3	0.05	20.00	0.03	325	002	0.03	262	007
4	0.06	16.67	0.01	324	001	0.02	252	009
5	0.07	14.29	0.06	324	002	0.05	320	005
6	0.08	12.50	0.05	323	002	0.09	242	009
7	0.09	11.11	0.09	324	001	0.07	273	006
8	0.10	10.00	0.05	324	001	0.03	267	008
9	0.11	9.09	0.02	325	001	0.01	249	005
10	0.12	8.33	0.01	324	002	0.01	194	008
11	0.13	7.69	0.01	324	001	0.01	278	004
12	0.14	7.14	0.02	325	001	0.02	309	005
13	0.15	6.67	0.02	324	001	0.02	311	002
14	0.16	6.25	0.13	323	001	0.10	308	002
15	0.17	5.88	0.07	324	001	0.14	307	001
16	0.18	5.56	0.14	325	001	0.16	303	001
17	0.19	5.26	0.19	325	002	0.14	302	001
18	0.20	5.00	0.15	326	001	0.09	302	001
19	0.21	4.76	0.06	324	003	0.07	308	001
20	0.22	4.55	0.04	323	002	0.07	310	001
21	0.23	4.35	0.05	324	002	0.04	305	002
22	0.24	4.17	0.07	324	002	0.10	300	001
23	0.25	4.00	0.09	323	002	0.10	308	001
24	0.26	3.85	0.02	324	003	0.04	302	001
25	0.27	3.70	0.07	324	002	0.07	308	001

of one record of simulated data which are similar to those of Fernandes et al. [1988] are given in Table 3.2. In this record, essentially two wave trains were simulated. One wave train represented swell of approximately 11 s coming from 000°. The other represented swell of around 6 s coming from 120°. It is seen from Table 3.3 that BUOY-D-P computes the direction of both swells accurately. In the case of 1156DBP, we see that the mean direction of both swells is correct if we add ±180° to the computed direction. Additional computer runs showed the same feature. While BUOY-D-P reproduced wave directions correctly, 1156DBP directions showed an offset of 180°

We found that this offset in the 1156DBP output could be removed by just reversing the signs of the simulated heave series. The presence of the offset of 180° and the fact that 1156DBP uses (3.4) instead of (3.5), indicate that the heave series in the ENDECO observed data are actually inverted about the zero line. Thus, the observed offset is solely due to differing assumptions concerning the heave series.

Table 3.2 Characteristics of computer simulated wave data

Wave Train No.	Heave amplitude (m)	Tilt amplitude (deg)	Period (sec)	Initial phase (deg)	Wave direction (deg)
1	0.1143	1.07	10.64	85	000
	0.1524	1.37	11.10	85	000
	0.1143	0.99	11.60	85	000
2	0.1143	1.99	5.74	90	120
	0.1524	2.59	5.88	90	120
	0.1143	1.90	6.01	90	120

Since in the case of simulated data there is an offset of 180° between directions computed by BUOY-D-P and 1156DBP, we cannot but conclude that the apparent consistency in the results in the case of observed data is by chance only. Application of empirically obtained frequency dependent amplitude and phase corrections, as suggested by LeBlanc and Middleton [1982] and incorporated in 1156DBP, might show the offset in the case of observed data also.

When we ran 1156DBP with computer simulated data using either a mono-chromatic train, or a multi-chromatic wave train whose component sinusoids were all from just one uniform direction, we observed an artifact of a backward travelling wave located in the higher frequencies. With BUOY-D-P, such an artifact was not present. The artifact of a backward travelling wave was observed by LeBlanc and Middleton [1982].

For the record, we may mention that the paper of Brainard [????] is unpublished. A CD-ROM computer search through the Aquatic Sciences and Fisheries Abstracts (ASFA) database did not list this particular article, though it listed several articles by the same author, including some apparently earlier work and some apparently later work.

The work reported here on determination of the wave directional spectrum from an orbital following buoy using the digital band pass filter method has been published in Fernandes et al.

Table 3.3 Analysis of computer simulated wave data with characteristics given in Table 3.2. Number of points, 2048; sampling interval, 0.5 sec

Band No.	Centre Frequency (Hz)	Centre Period (sec)	Software BUOY-D-P			Software 1156DBP		
			Energy (m^2/Hz)	Dir (deg)	Std Dev (deg)	Energy (m^2/Hz)	Dir (deg)	Std Dev (deg)
1	0.03	33.33	0.00	053	084	0.00	233	001
2	0.04	25.00	0.00	043	059	0.00	219	001
3	0.05	20.00	0.00	033	050	0.00	203	001
4	0.06	16.67	0.00	024	031	0.00	194	001
5	0.07	14.29	0.00	016	013	0.01	187	001
6	0.08	12.50	0.10	005	003	0.05	182	001
7	0.09	11.11	3.41	001	002	2.33	180	000
8	0.10	10.00	0.18	354	002	0.05	180	001
9	0.11	9.09	0.00	342	006	0.00	197	003
10	0.12	8.33	0.00	334	036	0.00	289	005
11	0.13	7.69	0.00	349	072	0.00	317	003
12	0.14	7.14	0.00	131	020	0.00	318	003
13	0.15	6.67	0.00	128	003	0.00	315	003
14	0.16	6.25	0.09	122	001	0.05	310	006
15	0.17	5.88	3.30	120	000	2.26	307	010
16	0.18	5.56	0.21	119	001	0.11	199	009
17	0.19	5.26	0.00	115	002	0.01	148	006
18	0.20	5.00	0.00	112	006	0.01	133	003
19	0.21	4.76	0.00	110	007	0.00	125	001
20	0.22	4.55	0.00	108	011	0.00	117	001
21	0.23	4.35	0.00	106	012	0.00	115	000
22	0.24	4.17	0.00	105	013	0.00	114	000
23	0.25	4.00	0.00	103	018	0.00	109	000
24	0.26	3.85	0.00	102	010	0.00	109	000
25	0.27	3.70	0.00	102	009	0.00	107	000

[1994].

Chapter 4

SAR

Radar is an active microwave sensor that measures by remote sensing the backscatter from the sea surface and generates a 2-dimensional synoptic image of the wavy sea surface. When mounted on an aircraft or a satellite it is known as Side Looking Airborne Radar (SLAR) or Synthetic Aperture Radar (SAR) respectively. SAR can give a description of the waves over a large area, each image being as large as $100 \times 100 \text{ Km}^2$ in case of SEASAT and ERS-1 and ERS-2 satellites. The above satellites are polar orbiting satellites which give global, repetitive, day and night and all weather coverage. SAR is the modern method for determining the wave directional spectrum.

Some fundamental information about radars, including synthetic aperture radar, is given in Chapter 4.1. A review of literature on SAR is given in Chapter 4.2.

Gaussian smoothed SAR image spectra have been evaluated from 512×512 pixel sub-scenes of image mode ERS-1 SAR scenes off Goa, Visakhapatnam, Paradeep and Portugal. The two recently acquired scenes off Portugal showed the signature of swell of wavelength $\approx 200m$ and internal waves of wavelength $> 400m$. Only internal waves of wavelength $> 400m$ were seen in the scene off Goa observed on 11 March 1992. The scenes off Visakhapatnam and Paradeep did not show any wave like features, the latter appearing to be of "white noise" nature. Chapter 4.3 describes our analysis of the above SAR image data.

There exists a 180° ambiguity in wave direction observed from radar imageries. Based on the method of Atanassov et al. [1985], a computer program has been developed for removal of the 180° ambiguity by using two images of the same area separated by a time interval which is small compared to the period of the dominant waves. The computer program has been successfully tested with computer simulated images. Chapter 4.4 describes our work on the problem of removal of the 180° ambiguity.

The work reported here on the determination of Gaussian smoothed SAR image spectra from measured data off Paradip, Goa, Visakhapatnam and Portugal; and on the removal of the 180° ambiguity in wave direction from radar imagery is presented in Fernandes et al. [1999] which has

been communicated to “Photonirvachak”.

4.1 RADAR FUNDAMENTALS

Radar is an acronym for RAdio Detection And Ranging. Radars were developed during World War II for detecting enemy aircraft, specially at night. Radars use electromagnetic radiation (waves) in the microwave region of the spectrum to illuminate an object. All electromagnetic radiation travels at the same speed, the speed of light in free air, viz., $3 \times 10^{10} \text{ cm s}^{-1}$. Light is the visible part of the electromagnetic spectrum between the infrared and ultraviolet bands of the spectrum. The full electromagnetic spectrum which includes phenomena as diverse as X-rays, γ -rays, visible light, infrared heat rays, microwaves used in cooking as well as for terrestrial and satellite communication.

The velocity of light, c is given by

$$c = v\lambda$$

where v is the frequency and λ is the wavelength. Since the speed of light is constant, we see that the frequency is inversely proportional to the wavelength. Thus wavelength or frequency is the distinguishing feature of electromagnetic radiation.

Regardless of its frequency, all electromagnetic radiation behaves alike. For most purposes it behaves like waves. Just like waves it can be refracted, diffracted or polarized, and it is shifted in frequency on reflection from a moving object (Doppler Effect). The only difference is the distance or scale over which the phenomena operate. If all dimensions are scaled by the wavelength of the radiation, then light cannot be distinguished from radio waves, and textbooks of optics can as claimed by Stewart [1985] be used to predict the propagation of radio signals.

As suggested above, electromagnetic radiation can be divided into two classes. The lowest frequencies are known as the radio bands. Radio bands are characterized by coherent sources of radiation, with modulation rates that are a significant fraction of the frequency, and is received by equipment that observes the phase of the radiation. Table 4.1 gives the modern nomenclature of the different radio bands. In contrast with the radio bands, the highest frequencies are the light beams. Light beams are characterized by either incoherent sources of radiation or by coherent sources of radiation with relatively low rates of modulation, and are received by equipment that detect the square of the amplitude of the signal, rather than its phase [Stewart, 1985].

Common modes of polarization used include VV (Vertical polarization at transmission and Vertical polarization at reception), HH (Horizontal polarization at transmission and Horizontal polarization at reception), and right-hand and left-hand circular polarization.

Table 4.1 Modern nomenclature of radio frequency bands. Extracted from Stewart [1985]

Band	Frequency range	Metric subdivision	Adjectival designation
2	30 to 300 Hz	Megametric waves	ELF Extremely low frequency
3	300 to 3000 Hz		VF Voice frequency
4	3 to 30 KHz	Myriametric waves	VLF Very low frequency
5	30 to 300 KHz	Kilometric waves	LF Low frequency
6	300 to 3000 KHz	Hectometric waves	MF Medium frequency
7	3 to 30 MHz	Dekametric waves	HF High frequency
8	30 to 300 MHz	Metric waves	VHF Very High frequency
9	300 to 3000 MHz	Decimetric waves	UHF Ultra high frequency
10	3 to 30 GHz	Centimetric waves	SHF Super high frequency
11	30 to 300 GHz	Millimetric waves	EHF Extremely high frequency
12	300 to 3000 GHz	Decimillimetric waves	- Far infrared

Table 4.2 World War II nomenclature of microwave bands. Extracted from Stewart [1985]

Band	Frequency range [Gigahertz]	Band	Frequency range [Gigahertz]
P	0.225-0.390	K	10.90-36.00
L	0.390-1.550	Q	36.0-46.0
S	1.55-5.20	V	46.0-56.0
C	3.90-6.20	W	56.0-100.0
X	5.20-10.90		

Common modes of modulation are amplitude modulation (AM) and frequency modulation (FM), both of which are used in radio broadcasts. In amplitude modulation, the power of the carrier wave is varied in accordance with the message being carried, while in frequency modulation, the carrier frequency is varied in response to the message being carried. FM is used in satellite communication because FM requires less power for long range transmission, and is also unaffected by the problem of picking up static associated with AM. In FM the amount of information that can be relayed is given by the bandwidth, i.e., the frequency range of the carrier. For example a TV Message relayed in the frequency range 54 to 58.2 MHz, has a bandwidth of 4.2 MHz. This bandwidth is spread out to as much as 36 MHz for quality satellite broadcasts. Voice channels in contrast require a bandwidth of only 3 to 4 KHz for quality sound reproduction.

Microwaves penetrate through clouds and to some extent rain also [Ulaby et al., 1981].

As mentioned by Baylin et al. [1993] higher frequency radio waves have the potential for relaying larger quantities of information, because as the frequency increases, any given bandwidth becomes a smaller fraction of the FM carrier wave frequency. Microwave transmissions to satellites or between earth based line of sight relay stations are not susceptible to noise from atmospheric disturbances as are lower frequency transmissions. Several times a year for a period of 2–3 days short wave radios fail due to sun spot activity which disturbs the required reflection of these relatively low frequency waves by the ionosphere. Below frequencies of about 30 MHz, a radio wave will be reflected back from the ionosphere. Since microwave frequencies are far above 30 MHz, they easily pass through the ionosphere shield, whence their usefulness in satellite communication and earth observation.

Table 4.2 gives the nomenclature of the different bands that make up the microwave part of radio frequency bands. Besides being used in all types of radars including Synthetic Aperture Radar mounted on satellites, microwaves are also used in transponders on communication satellites. In the sport of cricket, radars are used to measure the speed of the ball delivered by a fast or medium fast bowler. It is common to talk of X-, C-, L-Band radars or S-Band transponders. Subband designations designated by lower case letters are less frequently used except in case of K-Band. For example K_u -Band relays in communication satellites typically uplink from 13.7 to 14.2 GHz and downlink from 11.7 to 12.2 GHz.

The Synthetic Aperture Radar, on board ERS-1 satellite operates (images) at C-Band. S-Band links are used to control the ERS-1 satellite: downlink telemetry reception and uplink telecommand to be performed by European Space Agency (ESA) earth stations. And the data transmission from ERS-1 to the earth stations is done in X-Band. The radar altimeter on ERS-1 operates at K_x -Band.

4.1.1 Doppler Effect

A property of electromagnetic radiation (EMR), which is utilized in radars is the Doppler Effect. As given in Suits [1983], if a source of EMR having a fixed frequency, ν , either approaches or recedes from an observer, the observer will receive radiation from the source at a different frequency, ν' , where ν' is greater than ν for approaching sources and is less than ν for receding sources. This alteration of EMR frequency caused by relative motion between source and observer is called *Doppler Effect* and is given by

$$\nu' = \frac{\nu(1 - \beta^2)^{1/2}}{1 - \beta \cos \theta}$$

where β is the ratio of the source velocity to the propagation velocity of EMR, and θ is the angle between the direction of motion of the source and the line connecting the source and the observer. When $\beta \ll 1$ as in the case of aircraft and satellites, the above equation becomes simply

$$\Delta\nu = \frac{\nu u}{c} \cos \theta = \frac{u \cos \theta}{\lambda}$$

where u is the relative velocity between source and receiver; c is the velocity of EMR, and λ is the wavelength of the EMR.

The total change in frequency from that emitted to that received back at the aircraft or satellite is twice as much as in a single Doppler shift and is given by

$$\Delta\nu = \frac{2u}{\lambda} \cos \theta \quad (4.1)$$

A derivation of (4.1) as given in Moore [1983] is reproduced below.

The cause of the Doppler shift is the change of the phase of the signal due to relative motion in addition to the normal change in phase due to transmission, i.e., propagation. The instantaneous phase shift of a signal returned to a radar, ϕ neglecting phase shifts in the reflection process, is given by

$$\phi = \omega_c t - \kappa_c(2R) = \omega_c t - 4\pi R/\lambda_c$$

where ω_c is the angular carrier frequency, κ_c is the carrier wavenumber and λ_c is the carrier wavelength.

If there is no relative motion, the angular frequency, ω , which is the rate of change of phase is given by

$$\omega = \frac{d\phi}{dt} = \omega_c$$

In presence of relative motion,

$$\omega = \omega_c - \frac{4\pi}{\lambda_c} \frac{dR}{dt} = \omega_c - \frac{4\pi u_R}{\lambda_c}$$

In terms of frequency f , and carrier frequency f_c , the above formula may be written as,

$$2\pi f = 2\pi f_c - \frac{4\pi u_R}{\lambda_c}$$

i.e.,

$$f = f_c - \frac{2u_R}{\lambda_c}$$

i.e., $f = f_c + f_D$, where the Doppler shift in frequency, f_D is given by (4.2),

$$f_D = -\frac{2u_R}{\lambda_c} \quad (4.2)$$

which is the same as (4.1). In the above derivation of (4.2), u_R is the relative velocity, or the rate of change of R . And the factor 2 in above equations is due to the round trip distance involved in radar. For Doppler Effect in one way transmission this factor is not present.

4.2 SAR REVIEW

The first Synthetic Aperture Radar (SAR) was flown aboard the short lived SEASAT, the first satellite dedicated to the study of the oceans. A review of SEASAT performance is given in the book edited by Allan [1983]. Allan's article therein reports that the SEASAT SAR imaged ocean waves, internal waves, slicks and streaks. Articles by D. W. S. Lodge and N. H. Kenyon therein reported that SEASAT SAR imaged large scale marine bedforms like sand banks and sand waves and was useful in identifying the direction of current flows and in indicating whether the flood or ebb current is dominant. One of SEASAT SAR mission's objectives was to detect sea and fresh water ice and to map snow cover.

Johannessen et al. [1994] report that ERS-1 SAR has imaged horizontal roll vortices in the atmosphere, atmospheric gravity waves, wind and current fronts, wind direction, rain cells, eddies,

sea ice, internal waves, slicks and surface wind waves, specially swell. SAR is also useful for ship detection.

Ocean waves are weakly imaged and can be recognized from SAR imagery from their fine “finger print” like signature. In contrast with ocean waves, internal waves and bathymetric features are more strongly imaged.

The mechanism for imaging of long ocean waves/ internal waves by all types of radar including ship radar, Side Looking Airborne Radar (SLAR) or Real Aperture Radar (RAR) mounted on aeroplanes, and Synthetic Aperture Radar (SAR) mounted on satellites, is by modulation of the back-scatter from short Bragg resonant capillary-gravity waves by the long gravity waves/ internal waves. For Bragg scattering to be effective the radar incidence angle with respect to the vertical is generally between 20 and 70°. At near zero degrees or nadir incidence, specular reflection dominates while at angles larger than 70°, “shadowing” effect dominates.

The theory of imaging of longer ocean waves by all types of radar is discussed in terms of the ‘Two-scale’ model in which the sea surface is treated as a superposition of short Bragg scattering ripples superimposed on the longer gravity waves and was pioneered by Wright [1968], Valenzuela [1968], Keller and Wright [1975] and Alpers and Hasselmann [1978]; and is applied locally in a reference system lying in the tangent plane (‘facet’) of the long waves. Three processes contribute to ocean wave imaging by radar, the first two of which are common to both RAR and SAR, while the third is a feature solely of SAR: [1] the changes caused by the long wave slope, in the effective angle of incidence relative to the local facet normal (electromagnetic interactions or tilt modulation), [2] the modulation of the energy of the short Bragg scattering ripples through interactions between the ripple waves and the long gravity waves (hydrodynamic interactions or modulation), and [3] the temporal variation in facet position and the Bragg scattering coefficients of the facets during the finite integration time in which SAR sees the facet (motion effects or velocity bunching). A review of the theory of imaging of ocean waves by SAR is given in Hasselmann et al. [1985].

Alpers and Hennings [1984] give a theory of imaging of underwater bottom topography by real and synthetic aperture radar, while Alpers [1985] gives the theory of imaging of internal waves by radar.

Being an active microwave sensor SAR has an all-weather, day/night capability. High resolution in range (across track) direction is achieved by transmitting very short pulses to illuminate the sea surface. High resolution in azimuthal (along track) direction is achieved by using the forward motion of the satellite to synthesize an aperture of very great length.

A review of work done on measurement of ocean waves from space is given in Beal et al. [1991].

Determination of the wave directional spectrum from image mode SAR imagery off the coast

of India has been previously reported by Kumar et al. [1996], Kumar et al. [1997], Sarma [1997] and Kumar et al. [1999]. Mahadevan et al. [1990] are the pioneers in India in the field of ocean wave imaging by SAR.

4.3 SAR MEASUREMENTS

Digital ERS-1 image mode SAR scenes off Paradeep (observed on 31 May 1996), Goa (11 March 1992) and Visakhapatnam (2 December 1997), were purchased from the National Remote Sensing Agency (NRSA), Hyderabad with the intention of studying the spatial evolution of directional ocean wave spectra. The NRSA supplied the scenes off Goa and Paradeep, including header and trailer files on 1/2" Computer Compatible Tape (CCT). The scene off Visakhapatnam was supplied on CDROM. The image data was 8-bit and comprised of 6801 lines each of 6680 pixels. The line/pixel spacing is 15m as given in the header files.

Monaldo and Lyzenga [1986] give the methodology for evaluating the directional ocean wave spectra of 512X512 or 256X256 pixel sub-scenes drawn from the full imagery, according to which the following steps of computation have to be performed: (i) fractional modulation; (ii) 2-dimensional Fourier transform, which transforms the data from spatial domain to wave number domain; (iii) a fourth-order stationary response correction, to make allowance for azimuthal and range fall off in energy; (iv) Gaussian smoothing with a 15X15 kernel; (v) speckle noise removal; (vi) tilt and velocity bunching modulation transfer function (correction). The spectrum obtained on performing each of the steps (ii) through (v) is known as the SAR image spectrum. The spectrum obtained on completion of step (vi) is known as the wave directional spectrum, viz., wave height spectrum or wave slope spectrum depending on whether normalization with wave number is done or not. It has been found prudent by Beal [1981] to perform Gaussian smoothing with a 3X3 kernel prior to step (iii) above so as to obtain stable results when stationary response correction is performed.

....

Figure 4.1 SAR full image off Paradeep on 31 May 1996



Figure 4.2 512X512 SAR sub-scene off Paradeep on 31 May 1996

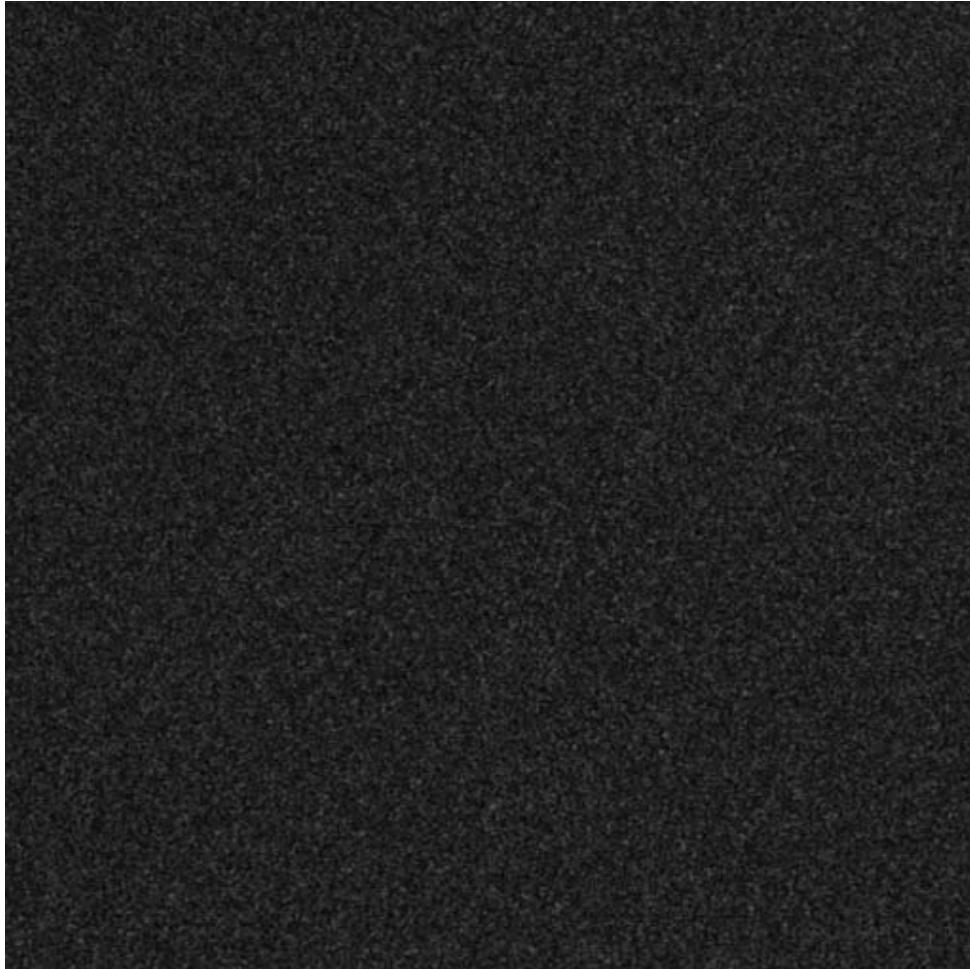


Figure 4.3 SAR image spectrum of 512X512 SAR sub-scene off Paradeep on 31 May 1996. Circles denote wavelengths of 50, 100, 200, 300 and 400m

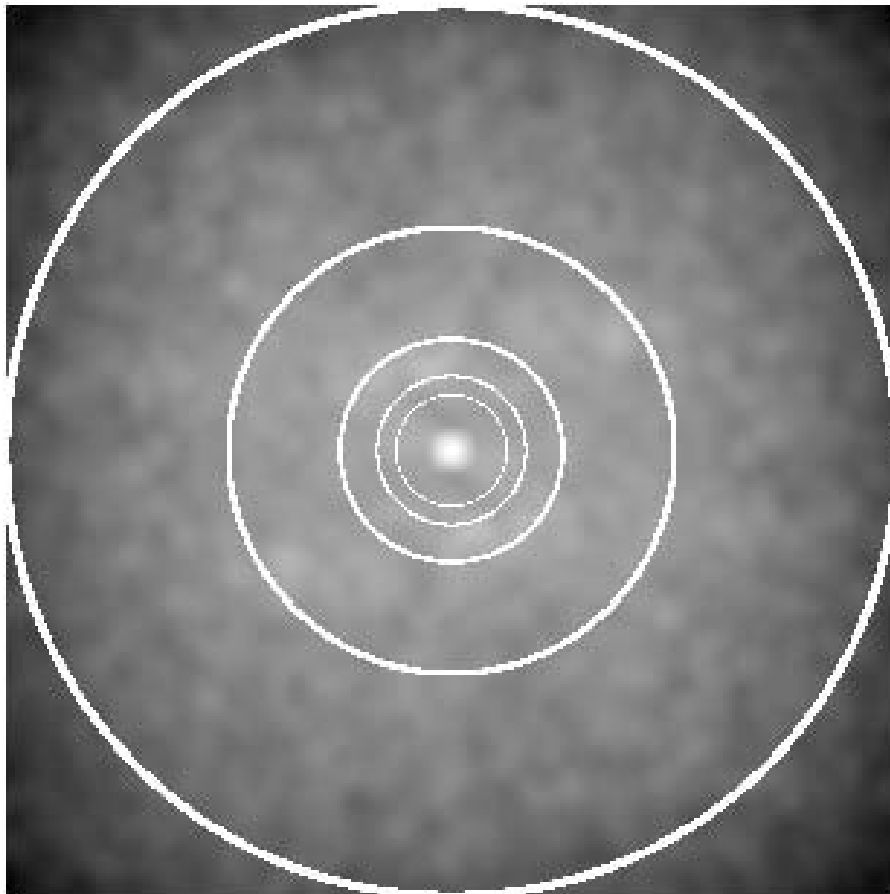


Figure 4.4 SAR full image off Goa on 11 March 1992

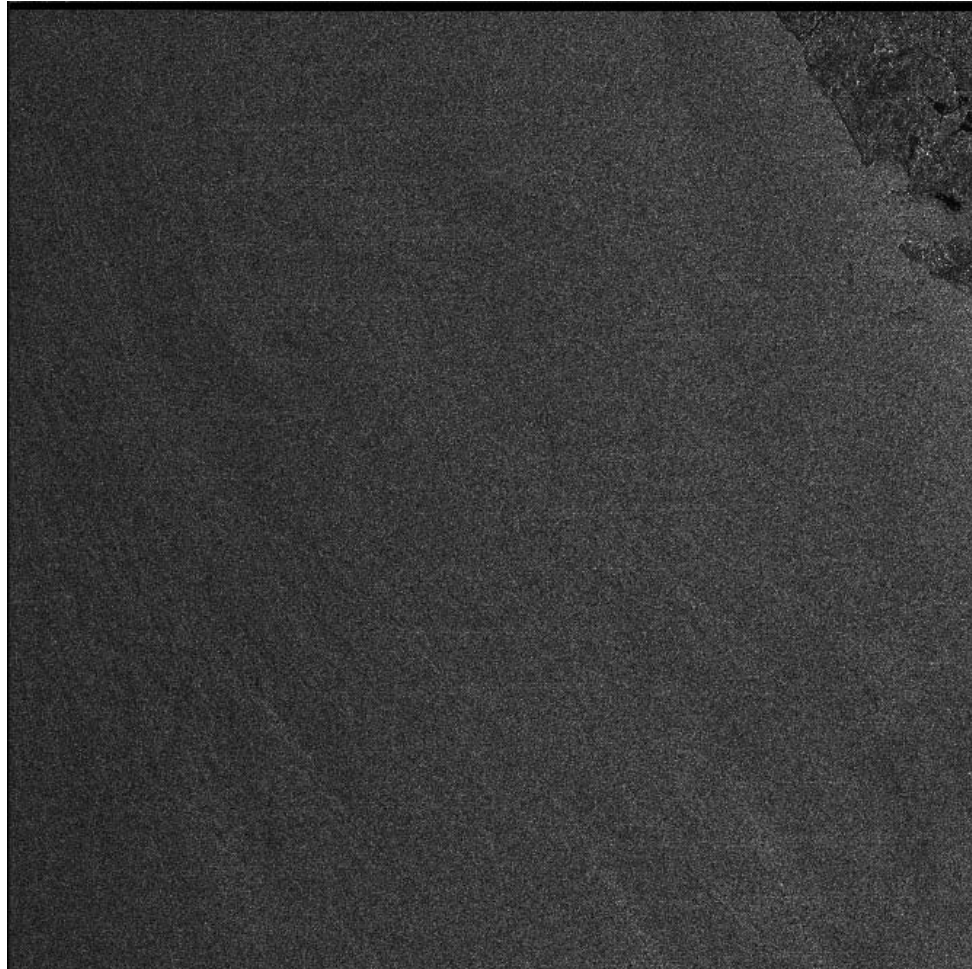


Figure 4.5 512X512 SAR sub-scene off Goa on 11 March 1992

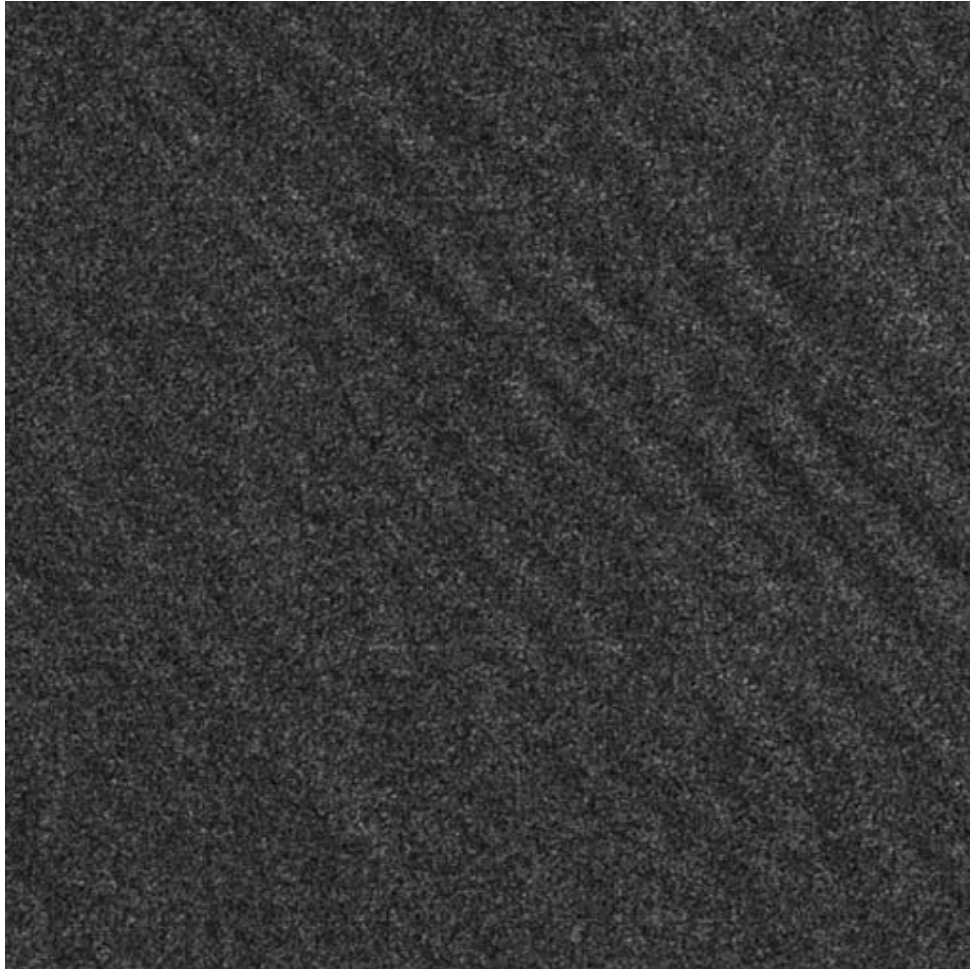


Figure 4.6 SAR image spectrum of 512X512 SAR sub-scene off Goa on 11 March 1992. Circles denote wavelengths of 50, 100, 200, 300 and 400m

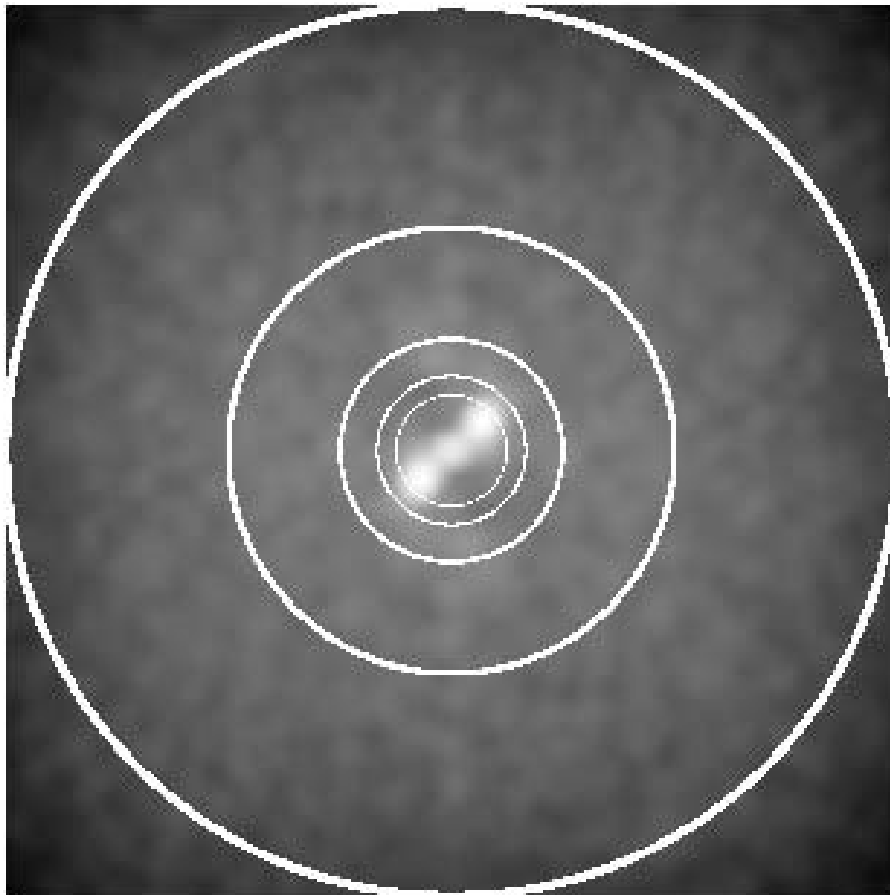


Figure 4.7 SAR full image off Visakhapatnam on 2 December 1997

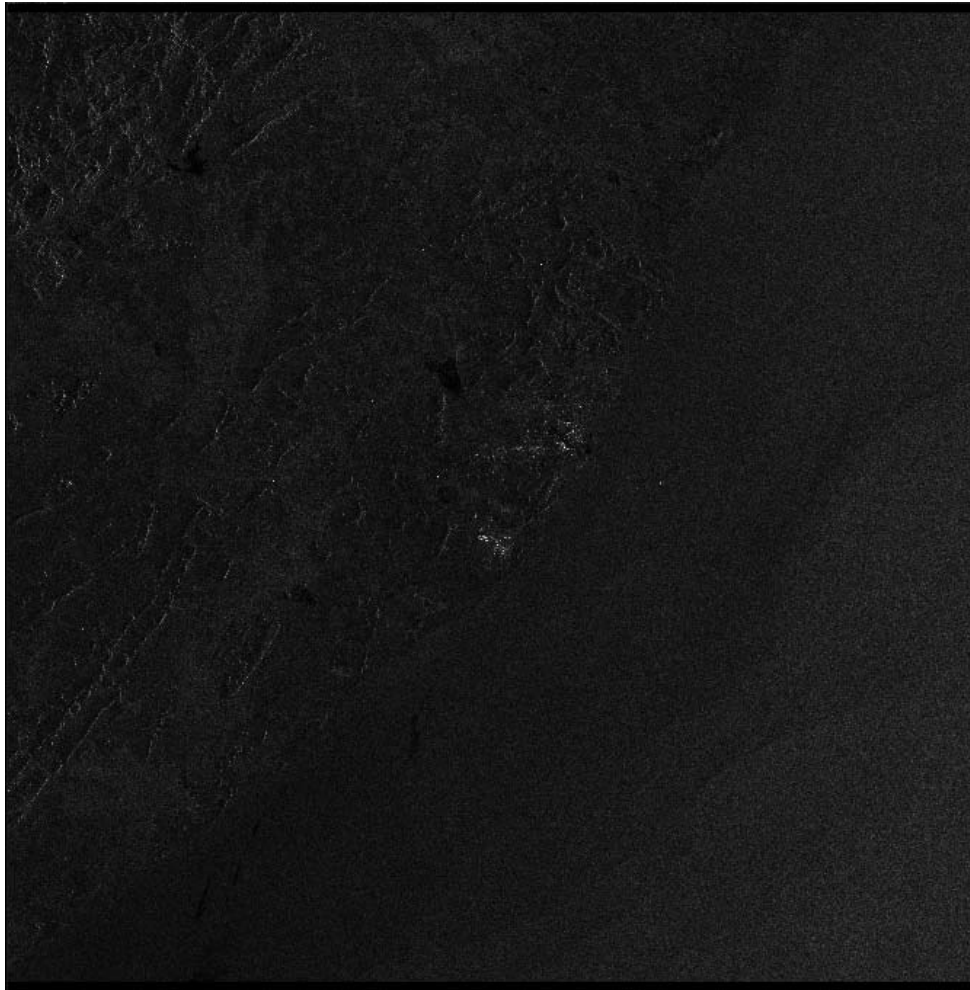


Figure 4.8 512X512 SAR sub-scene off Visakhapatnam on 2 December 1997

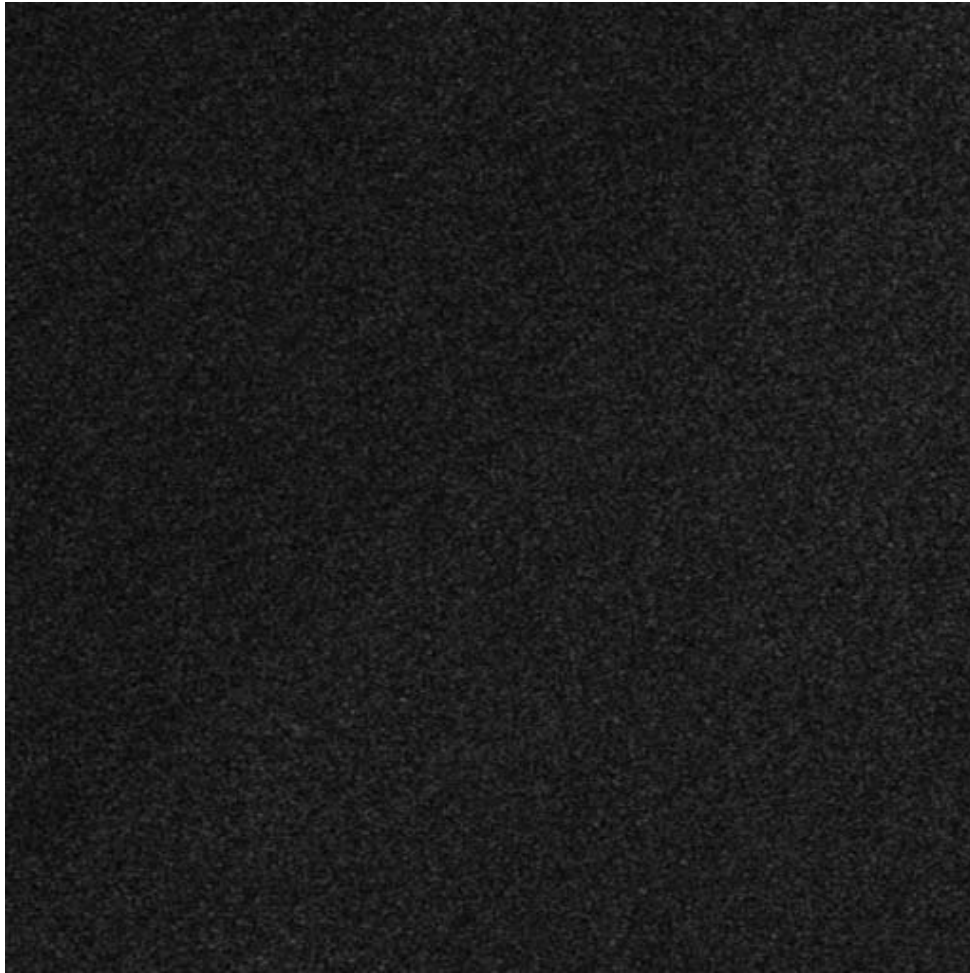


Figure 4.9 SAR image spectrum of 512X512 SAR sub-scene off Visakhapatnam on 2 December 1997. Circles denote wavelengths of 50, 100, 200, 300 and 400m

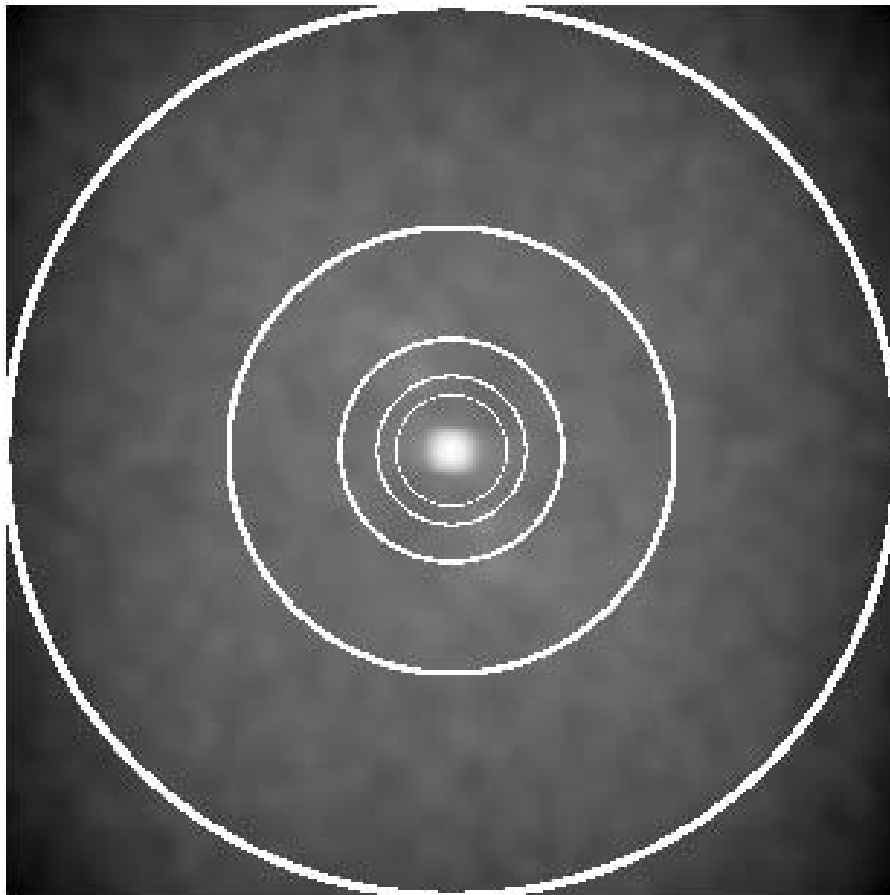


Figure 4.10 SAR full image off Portugal (p023-747)

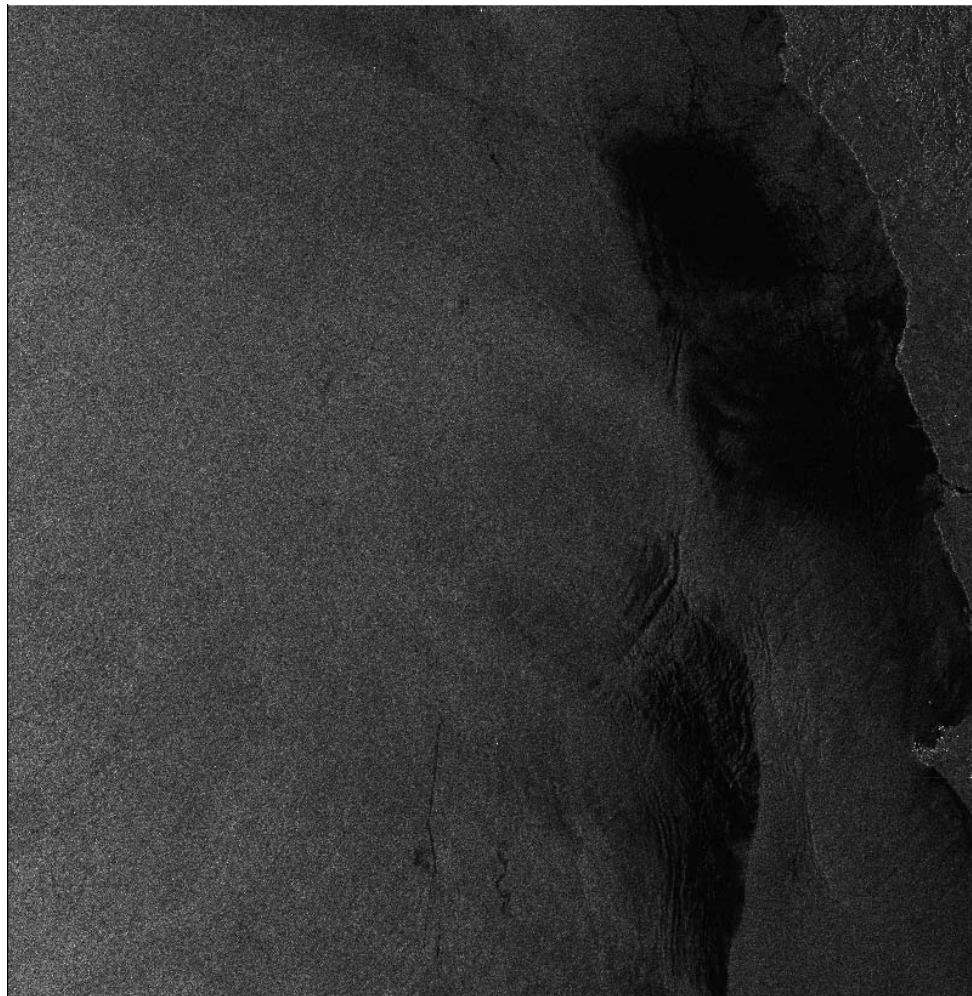


Figure 4.11 512X512 SAR sub-scene 'a' off Portugal (p023-747)

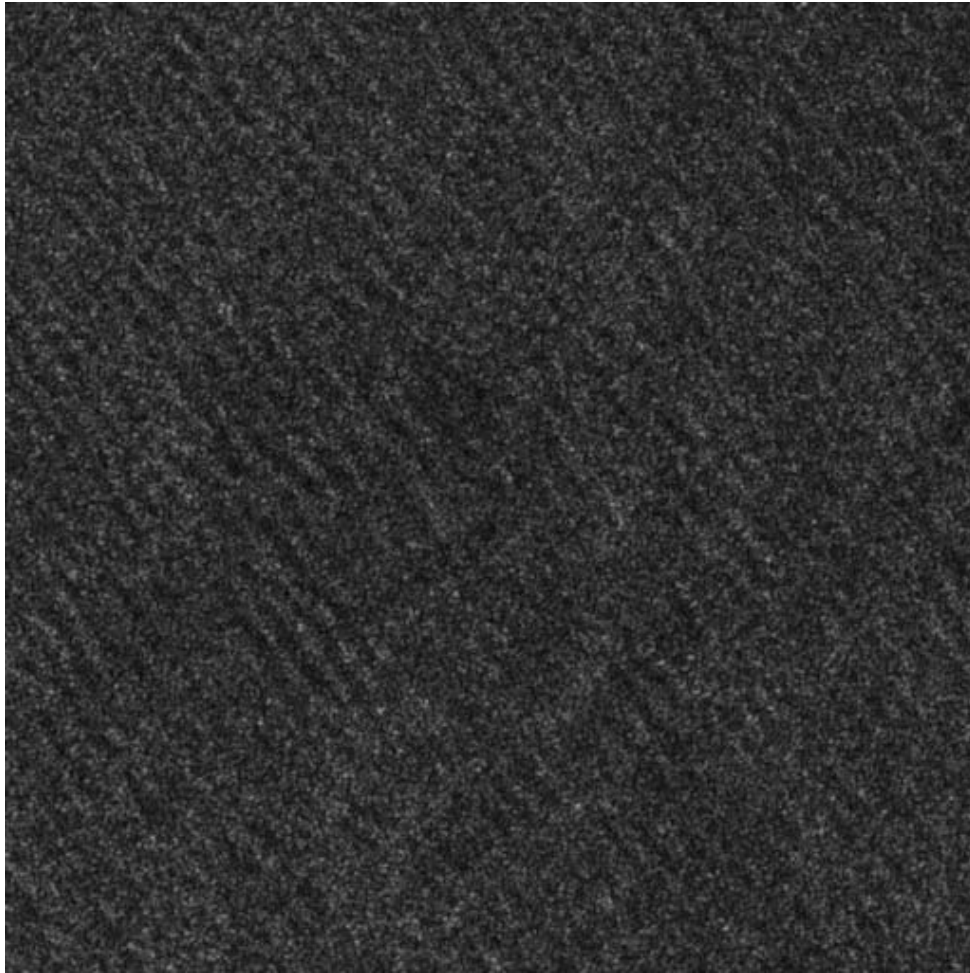


Figure 4.12 SAR image spectrum of 512X512 SAR sub-scene 'a' off Portugal (p023-747). Circles denote wavelengths of 50, 100, 200, 300 and 400m

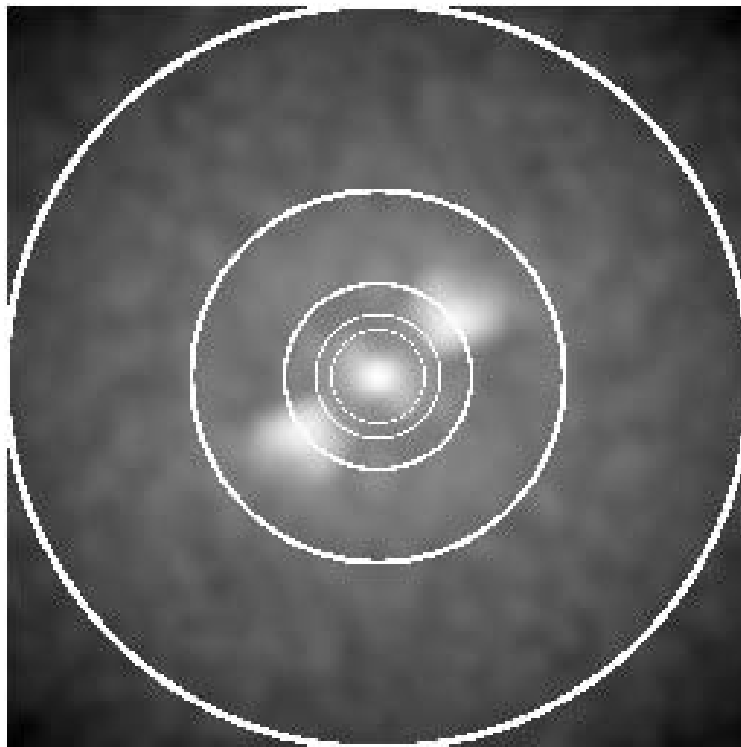


Figure 4.13 512X512 SAR sub-scene 'b' off Portugal (p023-747)



Figure 4.14 SAR image spectrum of 512X512 SAR sub-scene 'b' off Portugal (p023-747). Circles denote wavelengths of 50, 100, 200, 300 and 400m

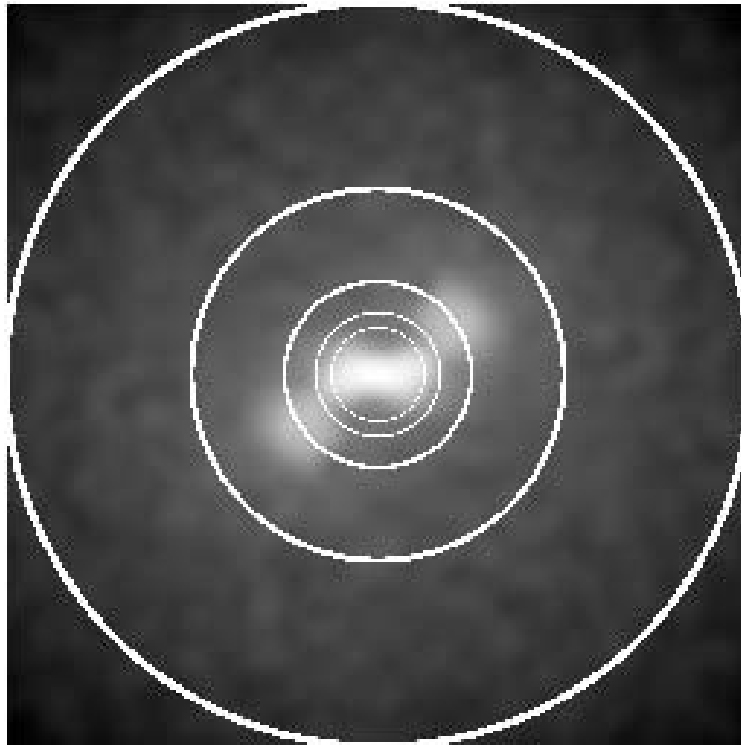


Figure 4.15 SAR full image off Portugal (p023-783)

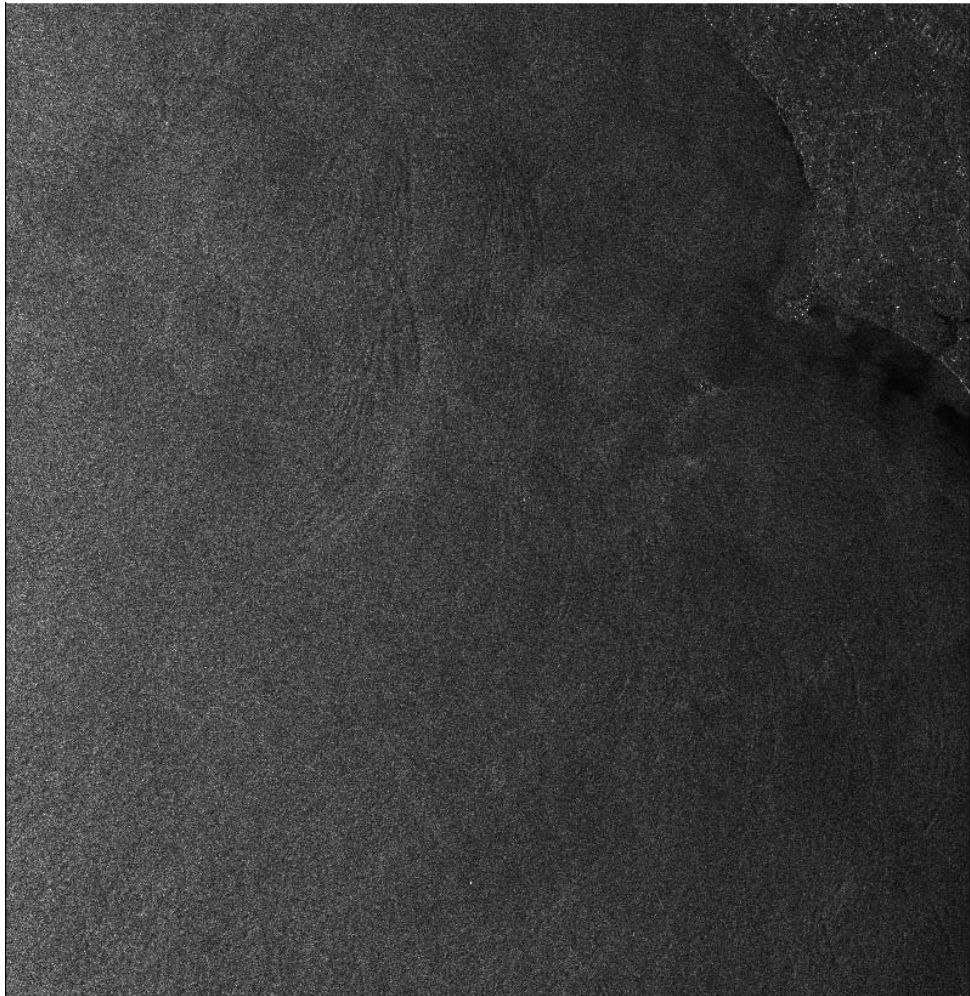


Figure 4.16 512X512 SAR sub-scene 'a' off Portugal (p023-783)

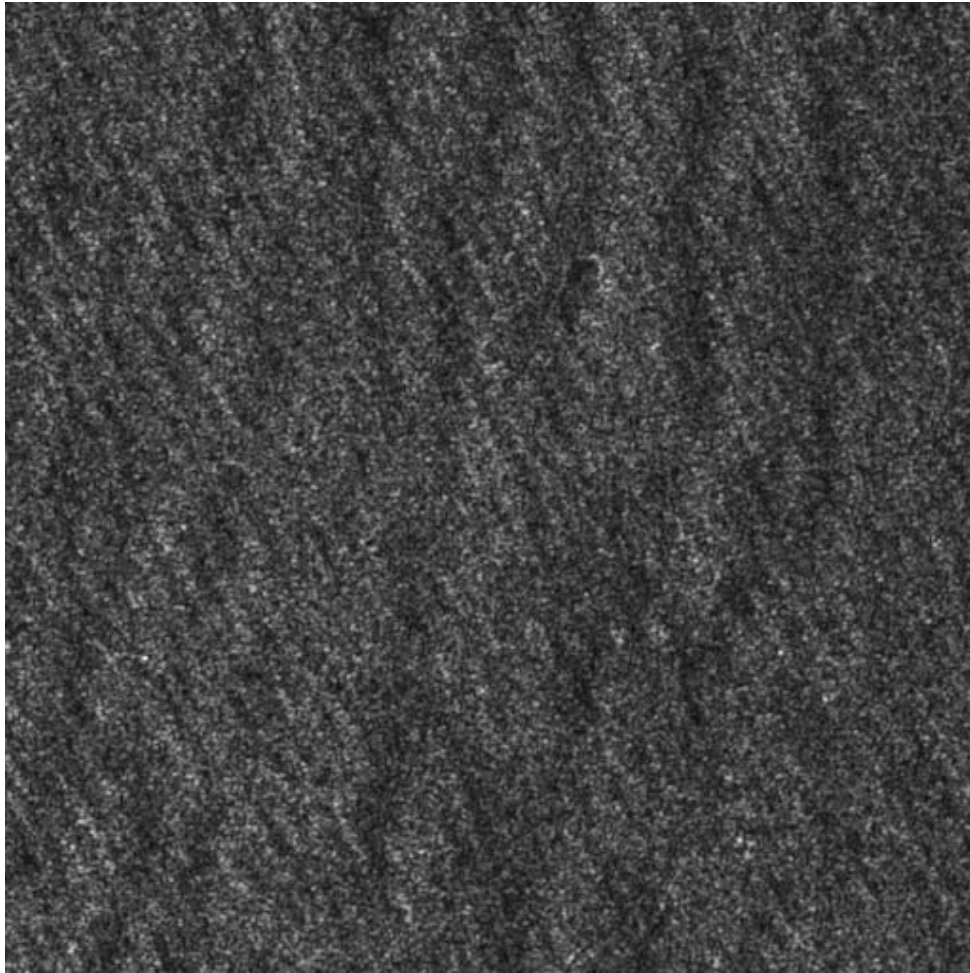


Figure 4.17 SAR image spectrum of 512X512 SAR sub-scene 'a' off Portugal (p023-783). Circles denote wavelengths of 50, 100, 200, 300 and 400m

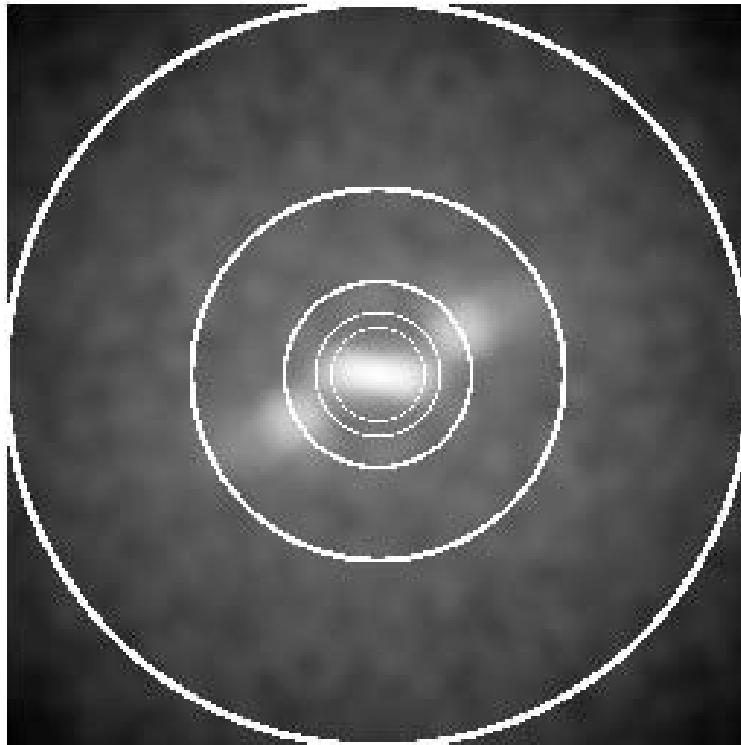


Figure 4.18 512X512 SAR sub-scene 'b' off Portugal (p023-783)

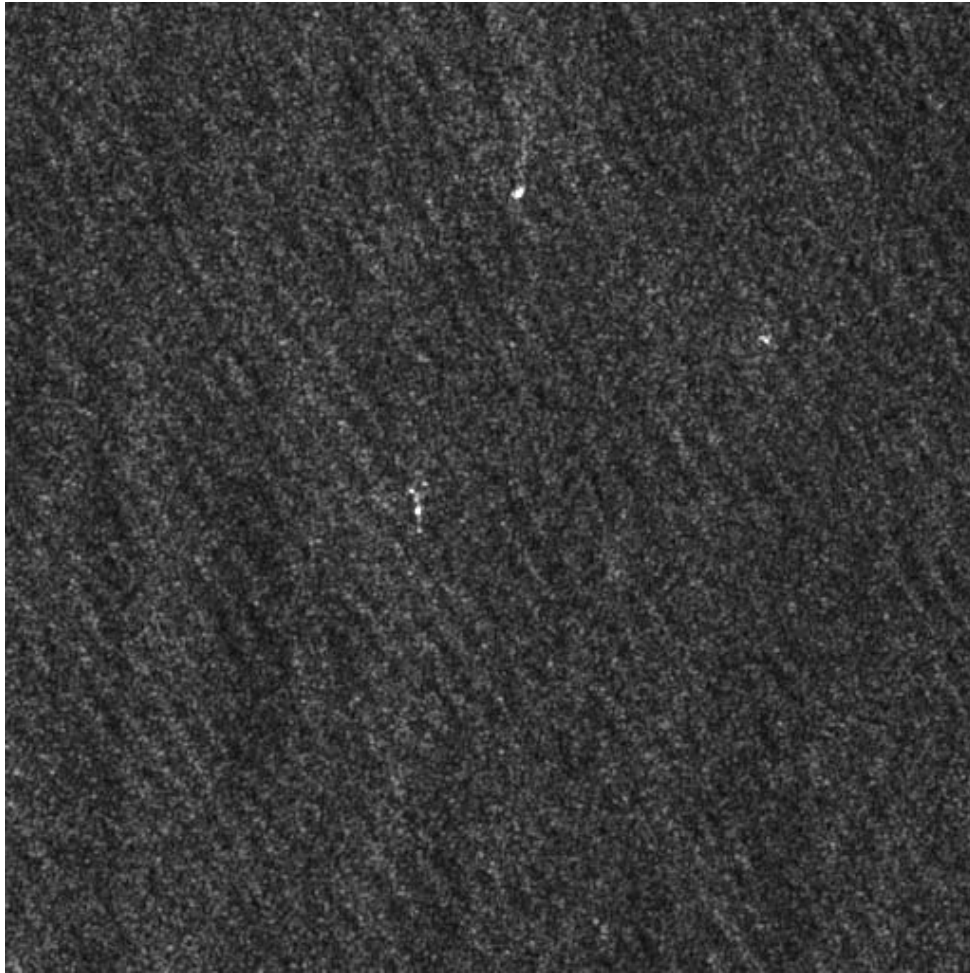


Figure 4.19 SAR image spectrum of 512X512 SAR sub-scene 'b' off Portugal (p023-783). Circles denote wavelengths of 50, 100, 200, 300 and 400m

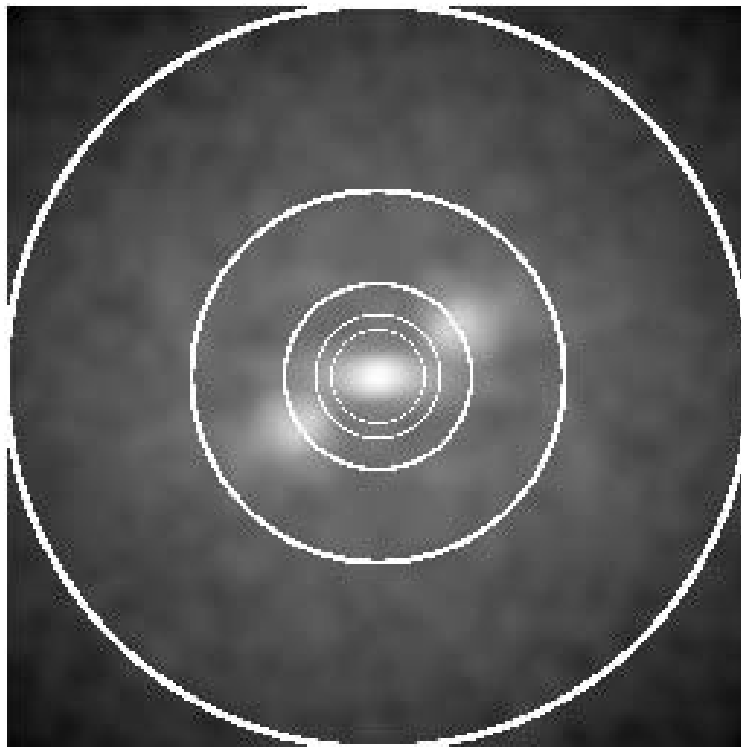


Table 4.3 Sea-truth (short term wave statistics) observed with an ENDECO wave directional buoy off Goa, and with a DATAWELL wave directional buoy off Visakhapatnam and Paradeep. H_s and T_z are the significant wave height (mean of the highest 1/3 waves) and the zero-crossing period (mean period) respectively; T_p and θ_p are the wave period and wave direction respectively corresponding to the principal peak in the energy spectrum; T'_p and θ'_p are the wave period and wave direction respectively corresponding to the secondary peak in the energy spectrum; † indicates time of wave buoy observation nearest to the time of ERS-1 satellite overpass

Location	Date	Time (IST)	H_s (m)	T_z (s)	T_p (s)	θ_p (°N)	T'_p (s)	θ'_p (°N)
Goa	11.3.92	0900	0.51	4.35	5.00	310	12.50	205
		1030	0.56	4.03	4.76	311	12.50	202
		1050†	0.57	3.77	5.00	320	12.50	228
		1200	0.57	3.63	5.26	316	12.50	263
		1300	0.59	3.33	5.00	314	12.50	242
Visakhapatnam	2.12.97	0530	0.55	5.41	15.38	162	5.88	132
		0900†	0.54	5.48	14.29	172	5.56	121
		1530	0.58	3.51	10.52	155	4.76	124
		1730	0.62	3.51	15.38	150	5.00	122
Paradeep	31.5.96	1245	1.66	5.56	8.33	194	5.56	118
		1545†	1.57	5.06	7.69	198	5.00	151
		1815	2.06	4.89	8.33	198	5.00	198
		2145	1.93	5.13	7.69	202	5.00	201

Fractional modulation comprises of subtracting the mean value of the back scatter from each element of the sub-scene and dividing the difference by the mean value. Stationary response correction is performed to make allowance for the well known azimuthal and range fall off of energy by using polynomials of even degree, the coefficients of which are evaluated separately from azimuthal and range spectral profiles of spectrally “white” sub-scenes, i.e., scenes which do not show any wave like features. Gaussian smoothing and speckle noise removal along with stationary response correction are meant to enhance the signal due to ocean waves. Speckle, or the graininess in the radar imagery is due to the fact that the image is obtained by a coherent source of radiation. Speckle is present in LASER (Light Amplification by Stimulated emission of Radiation) also. Tilt and velocity bunching modulation transfer functions are applied to take care of the imaging mechanism of ocean waves by SAR. It may be noted that in the scheme of Monaldo and Lyzenga [1986] the effect of another imaging mechanism, the hydrodynamic modulation transfer function is not taken into consideration as its amplitude is small compared to that of the tilt modulation transfer function.

Prior to January 1998 computer programs in FORTRAN on Microsoft DOS/Windows personal computers were developed and tested for (i) simulating images with sinusoidal waves; (ii) performing 2-dimensional Fourier Transform on the computer simulated images, and then view-

ing both the images as well as their Fourier Transforms using a computer program display.exe, kindly provided by Dr Raj Kumar of Space Applications Centre, Ahmedabad; and (iii) converting “direct access” image data files in the format used by display.exe, into PCX format, which could be viewed by using Microsoft Paintbrush/ Word/ Excel.

Analysis of digital ERS-1 image mode SAR data was started in January 1998, when a 32Mb ram, CDROM drive, 2.1Gb hard disk Pentium Debian Linux 1.3.1 personal computer, christened Aneerudh (Mathur), with X Windows environment and LAN connection to other computers including the SUN work station named Himalaya – was acquired.

The first scene that was successfully downloaded from CCT onto the hard disk of Himalaya was that off Paradeep (descending orbit 5813, path 857, row 201, scene centre 20.0630N 87.2920E) observed on 31 May 1996 at 1044 GMT, i.e., 1614 IST. A decimated image, i.e., an image formed by taking every tenth pixel/line was extracted from the downloaded full image, then converted to PCX format and then viewed on Aneerudh using ImageMagick, an image display package that displays an image just by invoking the command “display” followed by the name of the image file in any of the usual formats like PCX, BMP, TIFF, etc. The decimated image did not show any land part or any wave like features. Since the NRSA did not provide a glossy photograph of the full image along with the CCT, we extracted at random several 512X512 sub-scenes of area $7.68 \times 7.68 \text{ Km}^2$ and obtained Gaussian smoothed SAR image spectra, which showed that the Paradeep scene was entirely of “white noise” nature. Figure 4.1 shows the decimated full image at Paradeep. Figure 4.2 shows a 512X512 sub-scene with top left coordinates [pixel = 2910; scanline = 1020]. Gaussian smoothed SAR image spectrum for this sub-scene is given in Figure 4.3.

The next scene analyzed was that off Goa (descending orbit 3413, path 727, row 207, scene centre 15.2798N 73.3497E) observed on 11 March 1992 at 0534 GMT, i.e., 1104 IST. Sea truth was obtained with an ENDECO directional wave track buoy deployed for eight days (from 5 to 13 March 1992) off Candolim (Lat $15^{\circ}30'N$; Long $73^{\circ}44'E$) in a mean water depth of 14 metres. Fernandes et al. [1994] report that the buoy measurements showed that low wave conditions prevailed during the entire period of observation. The significant wave height was in the range 0.53–0.96m and the zero crossing period was in the range 4.36–5.98s. As computed by the ENDECO program 1156DBP.EXE, which computes spectral density and wave direction separately as a function of frequency using the digital band pass filtering method, the buoy observation at 1050 IST showed (see Table 4.3) that there were two main spectral peaks, both due to “swell” (waves generated by distant storms), the dominant peak being centred at 5.00s (direction $320^{\circ}N$, deep water wavelength $\approx 39m$), and the subsidiary peak was centred at 12.50s (direction $228^{\circ}N$, deep water wavelength $\approx 244m$). At 1100 hours on 10 March 1992, the swell direction corresponding to the dominant swell peak was roughly estimated by the author as $330^{\circ}N$ by visual observation. The glossy photograph of the full image accompanying the CCT, showed the presence of internal

waves. We selected several 512X512 sub-scenes, some of which were centred around the prominent internal waves in the glossy photograph, and obtained the Gaussian smoothed SAR image spectra, which showed only the signature of internal waves of wavelength $> 400m$. Figure 4.4 shows the decimated full image at Goa. Figure 4.5 shows a 512X512 sub-scene with top left coordinates [pixel = 2200; scanline = 4000], from an area showing the signature of internal waves. Gaussian smoothed SAR image spectrum for this sub-scene is given in Figure 4.6. Because of the well known azimuthal and range fall off with increasing wave number, as expected the signature of the the “swell” of 5.00s was not present in the SAR sub-scenes. Neither was the signature of the “swell” of 12.50s probably because the significant wave height was less than one metre. Gonzalez et al. [1979] from an analysis of SEASAT SAR imagery concluded that when the significant wave height is lower than 1–2m, the waves are not imaged. It may also be pointed out that the zero-crossing period, i.e., the mean wave period was $< 5s$ such that the waves could not be imaged by SAR.

The scene off Visakhapatnam (descending orbit 13686, path 821, row 204, scene centre 17.6727N 83.1856E) observed on 2 December 1997 at 0456 GMT, i.e., 1026 IST, showed some land part but no signature of any wave like features. Figure 4.7 shows the decimated full image at Visakhapatnam. Figure 4.8 shows a 512X512 sub-scene with top left coordinates [pixel = 4950; scanline = 4300]. Gaussian smoothed SAR image spectrum for this sub-scene is given in Figure 4.9.

Thus none of the the Gaussian smoothed SAR image spectra from the three scenes along the coast of India analyzed, viz., Paradeep, Goa and Visakhapatnam showed any ocean waves. As mentioned above, the reason for non-imaging of the buoy observed ocean waves (see Table 4.3), is probably due to the fact that the observed significant wave height $< 2m$ and the zero-crossing period during the satellite overpass is small ($< 6s$, $\lambda < 60m$). Therefore the visit of one of our colleagues, Dr. Y. V. B. Sarma to the Southampton Oceanographic Centre, U. K., was utilized to procure two ERS-1 digital image mode SAR scenes (p023-747 and p023-783) off Portugal, an area in which swell and internal waves were simultaneously imaged by SEASAT as reported by Allan [1983]. The SAR scenes off Portugal had 8201 lines each of 8006 pixels, the data being of 16 bits. The pixel/line spacing of the Portugal data is 12.5m as per the header files. Both the scenes off Portugal showed the signature of swell as well as internal waves.

Figure 4.10 shows the decimated full image of the scene p023-747 at Portugal observed on 15 June 1993 at 2254 GMT. Figure 4.11 shows a 512X512 sub-scene ‘a’ of area $6.4 \times 6.4 \text{ Km}^2$ with top left coordinates [pixel = 4280; scanline = 3770]. Gaussian smoothed SAR image spectrum of this sub-scene ‘a’ is given in Figure 4.12. Figure 4.13 shows a 512X512 sub-scene ‘b’ with top left coordinates [pixel = 6190; scanline = 5860]. Gaussian smoothed SAR image spectrum of this sub-scene ‘b’ is given in Figure 4.14.

Figure 4.15 shows the decimated full image of the scene p023-783 at Portugal also on 15 June

1993 at 2254 GMT, but 31s earlier than the previous scene (i.e., p023-747). Figure 4.16 shows a 512X512 sub-scene 'a' with top left coordinates [pixel = 4280; scanline = 3770]. Gaussian smoothed SAR image spectrum of this sub-scene 'a' is given in Figure 4.17. Figure 4.18 shows a 512X512 sub-scene 'b' with top left coordinates [pixel = 6190; scanline = 5860]. Gaussian smoothed SAR image spectrum of this sub-scene 'b' is given in Figure 4.19.

Gaussian smoothed SAR image spectra of the Portugal subscenes show swell of wavelength $\approx 200m$ with direction $\approx 40^\circ$ with respect to the range direction, and internal waves of wavelength $> 400m$ travelling in the range direction.

Analysis of the 512X512 pixel sub-scenes was restricted to just Gaussian smoothing of the raw SAR image spectra, to ensure that what was being enhanced was actually the ocean wave signal and not "noise". It is planned to develop subroutines for the other enhancements of the wave signal outlined by Monaldo and Lyzenga [1986], using the scenes off Portugal as they definitely contain ocean waves. If feasible it is also planned to try to adopt the more sophisticated strategy of inverting the SAR image spectrum by the method of Hasselmann and Hasselmann [1991] to yield the wave directional spectrum; the method being based on the iterative minimization of a cost function, which requires a model derived wave spectrum as a starting point. The original source code for the above inversion has already been procured. The method of Hasselmann and Hasselmann [1991] assumes a nonlinear mapping between the ocean waves and the image observed by SAR. In contrast Monaldo and Lyzenga [1986] assume a linear mapping between the ocean waves and the image observed by SAR.

4.4 REMOVAL OF 180 DEGREES AMBIGUITY

Some of the instruments used for obtaining radar imageries are (i) navigational radar mounted on ships (ii) SLAR (Side Looking Airborne Radar) mounted on aircraft and (iii) SAR (Synthetic Aperture Radar) mounted on satellites. These radar imageries are used to obtain information about the wave directional spectrum. However the wave directional spectra obtained from radar imageries suffer from a serious drawback, viz., the 180° ambiguity in the determination of the wave propagation direction. We may recall that a similar ambiguity in wave direction is present in case of linear arrays also. This drawback is usually overcome by assuming that the waves travel towards shore or downwind. The above assumptions therefore require additional knowledge of the wind field and the shore boundaries.

Atanassov et al. [1985] has proposed a method for removal of the 180° ambiguity which requires just two images of the same area separated by a time interval τ which is small compared to the wave period corresponding to the dominant wavelength in the imageries. The processing of the imageries is done in spectral (frequency or wave number) domain and uses the well known

wave dispersion relation:

$$\omega^2 = (2\pi f)^2 = \kappa g \tanh \kappa d \quad (4.3)$$

where $\kappa = (2\pi)/\lambda$, where κ and λ are the wave number and wavelength. Atanassov et al. [1985] successfully implemented their method both with computer simulated imageries as well as with actual PPI (Plan Position Indicator) imageries obtained with a ship radar. The method of Atanassov et al. [1985] has been applied to SLAR by Vachon and Raney [1989] and to SAR by Rosenthal et al. [1989] respectively. In SAR multi-look data (imagery) is essentially data observed at different times, the time interval being small. Multi-look data, which is normally used for reducing the “speckle” noise from SAR imagery, was used by Rosenthal et al. [1989] for removing the 180° ambiguity in wave direction.

Atanassov et al. [1985] have derived the following formula for unambiguously determining the image spectrum Δ as a function of the vector wave number \mathbf{k} :

$$\begin{aligned} \Delta_+(\mathbf{k}) = & 2\{1 - \cos[\omega(\mathbf{k}) + \omega(-\mathbf{k})]\tau\}^{-1} \\ & \cdot \{|\zeta(\mathbf{k}, t_1)|^2 + |\zeta(\mathbf{k}, t_2)|^2 \\ & - \text{Re}[\zeta(\mathbf{k}, t_1)\zeta^*(\mathbf{k}, t_2)\exp(i\omega(-\mathbf{k})\tau)]\} \end{aligned} \quad (4.4)$$

where τ is the time interval between two images observed at times t_1 and $t_2 (= t_1 + \tau)$, ζ is the 2-dimensional Fourier transform of the images with the superscript indicating the complex conjugate, and $i = \sqrt{-1}$.

We shall now derive a criterion which gives the maximum wavenumber for which Equation 4.4 can be used for unambiguously determining the image spectrum. It is assumed that

$$\omega(-\mathbf{k}) = \omega(\mathbf{k}) > 0$$

so that

$$[\omega(\mathbf{k})]\tau = 2\pi\tau/T \quad (4.5)$$

where T is the wave period. If we assume that $\tau < T/2$ (this is analogous to the criterion of Barber and Doyle (1956), $d < \lambda/2$ associated with wave directional arrays) and also assume that the images are taken in deep water so that the wave dispersion relation Equation 4.3 reduces to $\omega(\mathbf{k}) = \sqrt{\kappa g}$, then Equation 4.5 may be rewritten as follows

$$\sqrt{\kappa g} \tau < \pi$$

Making κ as the subject of the inequality, we obtain

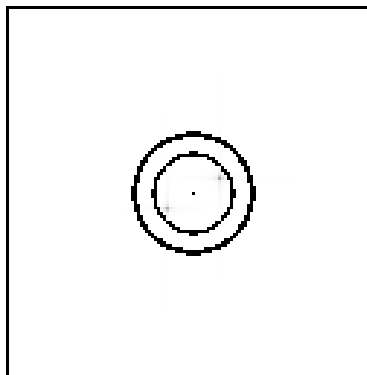
$$\kappa < (\pi/\tau)^2/g \quad (4.6)$$

Equation 4.6 gives an approximate wave number upper limit above which Equation 4.4 will fail to give unambiguous image spectra - we may emphasize that Equation 4.6 is exact in deep water.

Figure 4.20 Computer simulated image of a monochromatic wave field



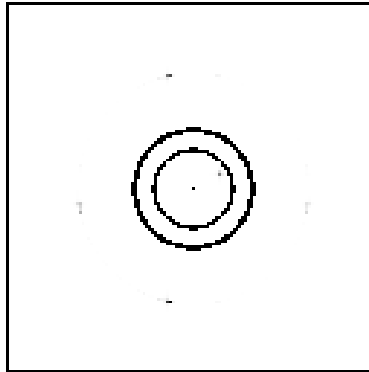
Figure 4.21 2-dimensional Fourier Transform of the computer simulated wave field showing the 180° ambiguity in wave direction



Multichromatic (i.e. with many frequencies) monochrome (i.e. in grey shades) images can be simulated in the computer using the following relation:

$$G(x_m, y_n, t) = \sum_{i=1}^I A_i \{1 + \cos[k_i(x_m \cos \alpha_i + y_n \sin \alpha_i) - \omega(k_i)t + \phi_i]\} \quad (4.7)$$

Figure 4.22 Unambiguous 2-dimensional Fourier Transform of the computer simulated wave field



for $m, n = 1, 2 \dots N$

where G gives the grey value in the range (0-255) in a square area of side $L = 676$ metres; $N = 128$; so that the image size is 128 X 128 pixels; $x_m = (m - 1)L/N$, $y_n = (n - 1)L/N$, are the x and y coordinates; t is the time; A_i are the amplitudes of the simulated waves having wavenumber κ_i and propagation direction α_i and initial phase ϕ_i ; κ_i satisfying the dispersion relation Equation 4.3

Using Equation 4.7 we simulated two monochromatic images (i.e. with single frequency) at time $t_1 = 0$ and $t_2 = 2.3$ seconds in $d = 30$ m water depth, so that $\tau = 2.3$ s, Other parameters chosen were $A_1 = 127$, $\alpha_1 = 30^\circ$, $\phi_1 = 10^\circ$; and $f_1 = 0.157$ Hz; which works out to $T_1 = 6.4$ s, $\kappa_1 = 0.997 m^{-1}$ and wavelength $\lambda_1 = 63$ m.

Figure 4.20 represents the radar image simulated at time $t_1 = 0$, which is indistinguishable to the naked eye from the image simulated at time $t_2 = 2.3$ (not shown). Figure 4.21 is the 2-dimensional Fourier Transform $\zeta(\mathbf{k}, t_1)$. Note that Figure 4.21 displays the correct wavelength, but there is as expected a 180° ambiguity in the wave direction. Figure 4.22 is the image spectrum computed using Equation 4.4. Figure 4.22 not only displays the correct wavelength, but also the unambiguously correct wave direction. The inner circle in Figure 4.22 depicts a wavelength of 50 m; the outer circle depicts a wavelength of 33 m, which corresponds to the maximum wave number given by Equation 4.6, for which Figure 4.22 gives correct results. The dot in Figure 4.22 representing the simulated wavelength of 63 m and wave direction of 30° , lies exactly along the the circle of wavelength of 63 m (not shown).